

X-Rays from Accelerated Ion Interactions

Vincent Tatischeff

Laboratory for High Energy Astrophysics
Goddard Space Flight Center, Greenbelt, MD 20771

Reuven Ramaty

Laboratory for High Energy Astrophysics
Goddard Space Flight Center, Greenbelt, MD 20771

and

Benzion Kozlovsky

Sackler Faculty of Exact Science, Tel Aviv University
Ramat Aviv, Tel Aviv, Israel

ABSTRACT

We have developed in detail the theory of X-ray line and continuum production due to atomic interactions of accelerated ions, incorporating in our calculations information from a broad range of laboratory measurements. We applied our calculations to the Orion region from which nuclear gamma-ray lines were observed with the COMPTEL instrument on *CGRO*. The accelerated particles which produce this gamma-ray emission via nuclear reactions also produce X-ray lines via atomic interactions. We predict strong line emission in the range from 0.5 to 1 keV, mainly due to de-excitations in fast O ions. While much of the diffuse X-ray emission observed with ROSAT from Orion could be due to accelerated ions, the current X-ray data do not provide unambiguous signatures for such an origin. If future observations with high spectral resolution would confirm the predicted X-rays, the combined analysis of the X-ray and gamma-ray data will set important constraints on the origin of the accelerated particles and their interaction model.

Subject headings: acceleration of particles–atomic processes–line:formation –ISM: individual (Orion)–gamma rays: theory–X-rays: general

1. Introduction

Strong gamma-ray emission in the 3-7 MeV range has been detected from the Orion molecular cloud complex with the COMPTEL instrument on the *Compton Gamma Ray Observatory* (*CGRO*; Bloemen et al. 1994, 1997). As the observed spectrum exhibits characteristic structures (Bloemen et al. 1997), this emission is most likely due to the superposition of nuclear gamma-ray lines, mainly the 4.44 MeV line from ^{12}C and the 6.13, 6.92 and 7.12 MeV lines from ^{16}O . Such line emission can only be produced by accelerated particle interactions. Gamma-ray emission at photon energies >30 MeV was also observed from Orion, with the EGRET instrument on *CGRO* (Digel, Hunter, & Mukherjee 1995). This gamma-ray emission is consistent with pion production and bremsstrahlung due to irradiation by standard Galactic cosmic rays (Digel et al. 1995). As such cosmic rays underproduce the observed line emission by at least three orders of magnitude, the gamma-ray line production in Orion must predominantly be a low energy cosmic ray phenomenon. Information on the spatial distribution of the gamma-ray line emission in Orion has come from both the COMPTEL and *CGRO*/OSSE observations. The extended nature of the emission seen in the COMPTEL map of Orion (Bloemen et al. 1997) could provide an explanation for the fact that so far it was not possible to confirm the COMPTEL results with OSSE (Murphy et al. 1996; Harris et al. 1998).

Based on the observed line widths, Bloemen et al. (1994) first suggested that the line emission is produced by accelerated C and O ions interacting with ambient H and He, rather than by accelerated protons and α -particles interacting with ambient C and O. More detailed analyses of the initial COMPTEL data have shown that a mix of the two processes could not be ruled out (Ramaty, Kozlovsky, & Lingenfelter 1995; Cowsik & Friedlander 1995). But, as the emission peaks in the more recent COMPTEL data do not appear at the line center energies for ^{12}C and ^{16}O de-excitations (Bloemen et al. 1997), a significant narrow-line contribution from accelerated proton and α -particle interactions seems to be excluded (Kozlovsky, Ramaty, & Lingenfelter 1997). This conclusion is also supported by energetic arguments, as the very large power deposited by the accelerated particles into the ambient medium in Orion is lowered by enhancing the C-to-proton and O-to proton abundance ratios (Ramaty et al. 1995; Ramaty, Kozlovsky & Lingenfelter 1996). Apart from the observed emission in the 3-7 MeV band, the COMPTEL observations revealed only upper limits at other gamma-ray energies (Bloemen et al. 1994, 1997). In particular, the upper limit on the 1-3 MeV emission sets constraints on the accelerated Ne-Fe abundances relative to those of C and O. The suppression of both the Ne-Fe and proton and α -particle abundances relative to C and O could be understood if the seed particles injected into an as-yet unknown particle accelerator (see Nath & Biermann 1994; Bykov & Bloemen 1994) come from the winds of massive stars or the ejecta of supernovae resulting from massive progenitors (Bykov & Bloemen 1994; Ramaty et al. 1995; Cassé, Lehoucq, & Vangioni-Flam 1995; Ramaty et al. 1996; Parizot, Cassé, & Vangioni-Flam 1997a). Ip (1995) and Ramaty et al. (1996) have also considered the possible acceleration of ions resulting from the breakup of interstellar dust.

The gamma-ray line production in Orion should be accompanied by a large ionization rate of

the ambient medium which could exceed the observed infrared luminosity (Cowsik & Friedlander 1995). This problem is alleviated if the gamma-rays are produced at cloud boundaries, but not in their interiors. The accelerated particles could have ionized $\sim 2 \times 10^4 M_\odot$ in 10^5 years (Ramaty 1996), a small fraction of the total available mass. It is thus possible that a large fraction of the power that accompanies the gamma-ray production is deposited in an ionized gas.

While the X-ray emission produced by low energy particle interactions is potentially a promising tracer of low energy cosmic rays in the Galaxy (e.g. Hayakawa & Matsuoka 1964), there are as-yet no astrophysical X-ray observations that unambiguously indicate the presence of such cosmic rays. The Orion region, however, has become an interesting target owing to the COMPTEL discovery of the nuclear gamma-ray line emission. A variety of processes lead to X-ray production by low energy ion interactions. Inverse bremsstrahlung (Boldt & Serlemitsos 1969) results from the interactions of fast ions and ambient electrons; secondary electron bremsstrahlung is produced by knock-on electrons accelerated in fast ion interactions (Hayakawa & Matsuoka 1964). Both of these processes lead to continuum X-ray emission. X-ray line emission results from atomic de-excitations in the fast ions following electron capture (Silk & Steigman 1969; Watson 1976; Pravdo & Boldt 1975; Bussard, Ramaty, & Omidvar 1978) and in ambient ions following inner-shell vacancy creation. The latter process has not yet been applied to astrophysics. Dogiel et al. (1997) have recently considered the X-ray emission that should accompany the gamma-ray line production in Orion. They have only considered the secondary electron bremsstrahlung and concluded that the 0.5-2 keV emission that accompanies the observed gamma-ray line emission from Orion will exceed the upper limits that they derived using ROSAT observations. We have subsequently taken into account both continuum processes and line emission from de-excitations in fast O (Ramaty, Kozlovsky, & Tatischeff 1997a) and showed that, even though the inverse bremsstrahlung is more important than the secondary electron bremsstrahlung, the total X-ray continuum emission from Orion is not inconsistent with the Dogiel et al. (1997) derived ROSAT upper limit. On the other hand, we showed that a conflict may exist between that ROSAT upper limit and the X-ray line emission following electron capture onto fast O nuclei. However, as we suggested, this conflict could be resolved if the X-ray and gamma-ray lines are produced in an ionized medium or if the current epoch accelerated particle spectrum is suppressed at low energies, for example by energy losses.

In this paper we present detailed calculations of X-ray continuum and line production by accelerated particle interactions. The bulk of our treatment is for a steady state, thick target model with a neutral ambient medium. This is the standard model in which most of the gamma-ray calculations have been carried out (e.g. Ramaty et al. 1996). But we have also investigated the effects of an ionized ambient medium and a time-dependent model, as these modifications could have important consequences on the predicted X-ray to gamma-ray production ratio. In our treatment of the continuum, we have supplied the details of the calculations and we have improved the employed cross sections, thereby confirming our previous preliminary results (Ramaty et al. 1997a). We have greatly expanded our treatment of X-ray line emission. We have investigated

in detail the atomic physics relevant to line emission from de-excitations in fast O, checking our theoretical calculations against laboratory data whenever available. We then expanded the treatment to the other abundant accelerated ions (C, N, Ne, Mg, Si, S and Fe), and we have also calculated the X-ray line emission produced in ambient ions following inner-shell vacancy creation by the accelerated particles. We have used the ROSAT all-sky survey (Snowden et al. 1995) to derive the X-ray count rates from the Orion region that could be associated with accelerated particle interactions; the implied fluxes are quite different from the upper limit given by Dogiel et al. (1997). The unambiguous future detection of the predicted X-rays produced by accelerated particles in Orion, and potentially elsewhere in the Galaxy, should provide important new insights into the origin of the low energy cosmic rays whose presence in Orion is revealed by the COMPTEL gamma-ray line observations.

2. Interaction model

We consider a steady state, thick target interaction model in which accelerated particles with given energy spectra and composition are injected at a constant rate into an interaction region of solar composition and produce atomic and nuclear reactions as they slow down to energies below the thresholds of the various reactions. We perform the calculations in a neutral ambient medium. In §5.1 we discuss the expected modifications for a partially ionized medium and in §5.2 the modifications that could result if the accelerated particle population is allowed to evolve in time.

The thick target X-ray and gamma-ray production rates can be written as (e.g. Ramaty et al. 1996)

$$Q = \frac{1}{(1 + 1.8 \frac{n_{He}}{n_H}) m_p} \sum_{ij} A_i \frac{n_j}{n_H} \int_0^\infty \frac{\sigma_{ij}(E_n) dE_n}{Z_i^2 (eff) (\frac{dE}{dx})_{p,H}} \int_{E_n}^\infty \frac{dN_i}{dt}(E'_n) dE'_n . \quad (1)$$

Here i and j range over the accelerated and ambient particle types that contribute to the atomic or nuclear product considered; E_n is the accelerated particle energy per nucleon; $\frac{dN_i}{dt}(E_n)$ is the differential injection rate of projectiles of type i into the target region, measured in particles (MeV/nucleon) $^{-1}$ s $^{-1}$; $\sigma_{ij}(E_n)$ is the cross section for the particular reaction considered; $(\frac{dE}{dx})_{p,H}$ is the proton energy loss rate per g cm $^{-2}$ in ambient neutral H; Z_i , A_i and $c\beta_i$ are the nuclear charge, mass and velocity of projectiles of type i ; $Z_i(eff) = Z_i[1 - \exp(-137\beta_i/Z_i^{2/3})]$ is the equilibrium ionic charge in a neutral ambient medium (Pierce & Blann 1968); n_H , n_{He} and n_j are the densities of ambient H, He and constituent j ; and m_p is the proton mass.

We perform calculations with an accelerated particle source spectrum of the form (Ramaty et al. 1996)

$$\frac{dN_i}{dt}(E_n) \propto E_n^{-1.5} e^{-E_n/E_0} . \quad (2)$$

The power law $E_n^{-1.5}$ is appropriate for strong shock acceleration in the nonrelativistic region. The exponential cutoff, introduced by Ellison & Ramaty (1985) for solar flare acceleration, could

be caused by a finite shock size or finite acceleration time. In the case of Orion, arguments of energetics require a hard spectrum in the nonrelativistic region (Ramaty et al. 1996), such as that given by equation (2) with as high a value for the turnover energy ($E_0 \lesssim 100 \text{ MeV/nucleon}$) as allowed by the requirement that the high energy gamma-ray emission due to pion decay not be overproduced (Tatischeff, Ramaty, & Mandzhavidze 1997). While such values of E_0 are reasonable for solar flares, it is not clear that in the case of strong shock acceleration the relevant geometry and time scales for Orion will lead to a cutoff at a sufficiently low energy. Alternatively, the acceleration in the nonrelativistic region could be stochastic due to turbulence or an ensemble of weak shocks (Bykov & Fleishman 1992; Bykov 1995). This mechanism predicts an even harder nonrelativistic spectrum (E_n^{-1}), and one which steepens at higher energies where the acceleration is due to single weak shocks. Because of its simplicity, we shall use equation (2) in our subsequent calculations, allowing E_0 to vary from 10 to 100 MeV/nucleon.

We employ three different compositions for the accelerated particles: CRS and WC (Ramaty et al. 1996, table 1); and OB (Parizot et al. 1997a, table 1 the OB/0.02 column). CRS is the composition of the current epoch Galactic cosmic-ray sources, WC is the composition of the winds of Wolf-Rayet stars of spectral type WC, and OB is the average composition of the winds from OB associations. The C and O abundances relative to protons, α -particles and heavier metals are much higher for the WC case than those for the CRS case. For the OB case, these abundances ratios are intermediate between those of the CRS and WC cases.

3. X-ray continuum emission

Energetic ions produce continuum X-ray emission via both inverse bremsstrahlung (Boldt and Serlemitsos 1969, hereafter IB) and bremsstrahlung from secondary knock-on electrons (see also Anholt 1985). For nonrelativistic protons interacting in stationary H, the inverse bremsstrahlung cross section is identical to the bremsstrahlung cross section for electrons of kinetic energy $(m_e/m_p)E$ also interacting in stationary H; here m_e and m_p are the electron and proton masses respectively and E is the proton kinetic energy. We used equation 3BN from Koch and Motz (1959). For heavier ions interacting in an ambient medium consisting of heavier atoms, we replaced the proton energy E by the energy per nucleon of the projectile, E_n , and multiplied the cross section by $Z_i^2 Z_j$, where Z_i and Z_j are the fast ion and ambient atom charge numbers, respectively.

The secondary electrons are knock-on electrons which subsequently produce bremsstrahlung by interacting with the ambient atoms. The angle averaged differential X-ray production cross section for secondary electron bremsstrahlung (SEB) can be written as

$$\frac{d\sigma}{d\epsilon}(E_n, \epsilon) = \frac{Z_i^2 Z_j^2}{m_p} \int_{\epsilon}^{\infty} \frac{d\sigma_{BR}}{d\epsilon}(E_e, \epsilon) \frac{dE_e}{\left(\frac{A_j}{Z_j}\right) \frac{dE_e}{dx}(E_e)} \int_{E_e}^{\infty} \frac{d\sigma_{KN}}{dE_e}(E_n, E'_e) dE'_e, \quad (3)$$

where $(d\sigma_{KN}/dE_e)(E_n, E'_e)$ is the knock-on cross section for the ejection of an electron of energy E'_e by a proton of energy E_n interacting with H (Chu et al. 1981 with corrections at high energies

from Rudd et al. 1966 and Toburen and Wilson 1972); $(d\sigma_{BR}/d\epsilon)(E_e, \epsilon)$ is equation 3BN of Koch and Motz (1959) for electrons of energy E_e interacting with H and radiating a photon of energy ϵ ; and dE_e/dx is the electron energy loss rate per g cm⁻² in the ambient medium (Berger and Seltzer 1982). Since dE_e/dx scales approximately as Z_j/A_j , where A_j is the target atomic number, the overall cross section scales as $Z_i^2 Z_j^2$. In comparison, the IB cross section scales as $Z_i^2 Z_j$.

In Figure 1a we show our calculated IB and SEB cross sections for protons interacting in H and Be, and compare our results for Be with experimental data (Chu et al. 1981). We see that while for the Be target the two calculated cross sections are approximately equal, for the H target the IB cross section dominates (except at the highest energies). This is the direct consequence of the dependencies of the cross sections on the target charge number Z_j derived above. In the case of the Be target we get good agreement with the experimental data at 90°, the discrepancy of less than a factor of 2 possibly being due to our angle averaging and contaminations in the experiment, for example Compton scattering of gamma rays in the Be target.

Using equation(1) we calculated the ratio of the IB and SEB productions as a function of photon energy for an ambient medium with solar abundances, for various values of the characteristic energy E_0 [Eq. (2)], and various accelerated particle compositions. We find that, as expected, the ratio is practically independent of the accelerated particle composition. We thus show results only for the CRS composition (Figure 1b). We see that, except at the highest energies, the IB-to-SEB ratio ranges from about unity to almost 10, depending on the photon energy and the spectrum of the accelerated particles (i.e. the value of E_0).

4. X-ray line emission

X-ray line emission results mainly from $2p$ to $1s$ and $3p$ to $1s$ transitions, in either the fast ions or the ambient atoms, giving rise to $K\alpha$ and $K\beta$ X-rays respectively. In the case of the fast ions, the $2p$ and $3p$ states can be populated either by electron capture from ambient atoms (i.e. charge exchange) or by excitation of $1s$ electrons for ions having one or two electrons. We neglected the $K\alpha$ and $K\beta$ X-ray production from fast ions having more than two electrons as the collision energy in this case is mostly given to the outer electrons and thus not giving rise to a significant K-shell electron excitation. The fast ions also produce K-shell vacancies in the ambient atoms (Garcia, Fortner, & Kavanagh 1973; Cahill 1980). We first consider the K X-ray production in fast O.

4.1. K X-rays from fast oxygen

X-ray line production from fast O has already been treated by Pravdo & Boldt (1975) and Watson (1976). The latter has considered the interaction of energetic O with only ambient hydrogen. But, as shown by Bussard et al. (1978) for $K\alpha$ X-ray emission from fast Fe, heavier

ambient elements cannot be neglected despite their lower abundances because of the strong dependence of the charge-exchange cross section on the charge of the target nucleus. Pravdo & Boldt (1975) have taken into account the contributions of the heavier elements, but as we shall see, their use of the Oppenheimer-Brinkman-Kramers (OBK) approximation for the charge-exchange cross section in the form presented by Schiff (1954) gives a poor description of the available experimental data.

The main lines produced by fast O ions result from the $2p$ to $1s$ transitions in H- and He-like projectiles giving rise to $K\alpha$ X-rays at 0.65 keV (O VIII line) and 0.57 keV (O VII line), respectively (Matthews et al. 1973). In addition, we considered the $3p$ to $1s$ transitions, which give rise to non-negligible $K\beta$ X-rays at 0.77 and 0.67 keV, for H- and He-like O ions, respectively (Hopkins et al. 1974).

4.1.1. Charge Exchange cross section

Even though the OBK cross section is known to exceed the experimental data by a factor of 10 or more in certain cases, it predicts quite accurately the shape of the measured cross sections versus energy (e.g. the review of Belkić, Gayet, & Salin 1979). Schiff (1954) has derived a general form for the OBK cross section for capture of electrons by fast ions from the ground state of a H-like ion. This formula is not appropriate to describe electron capture from heavy targets containing many atomic electrons. Nikolaev (1967) has extended the OBK cross section to heavy ion charge exchange, taking into account the complete atomic configuration of the target atoms. He also derived a semi empirical scaling relation in order to adapt his theoretical result to experimental data. But subsequent measurements have shown that a discrepancy of a factor of 2-3 remains between theory and experiment in some cases (e.g. Ferguson et al. 1973). Thus, instead of using the Nikolaev (1967) semi empirical factor, we normalized the Nikolaev cross section to experimental data. In the Nikolaev formalism we used the binding energies of the target electrons from Sevier (1979), and the Slater (1930) rules to take into account the external screening of the nuclear charge by the inner shells.

A compilation of experimental cross sections is shown in Figure 2, together with theoretical calculations. The closed symbols show K X-ray production cross sections due to charge exchange for fast fully stripped O and F interacting with neutral H, He, Ar and Kr. The solid curves are our fits to these data obtained by using the Nikolaev (1967) formalism to calculate the capture cross sections $\sigma_{n \geq 2}$ to all states with principal quantum number $n \geq 2$. To take into account the captures which populate the $2s$ metastable state (which does not lead to K X rays), we reduced $\sigma_{n \geq 2}$ by 4% based on the calculations of Guffey, Ellsworth & Macdonald (1977) for O and F projectiles in He. This small correction, however, is negligible in comparison with the overall normalizing factor of 0.1 that we applied to the calculated curves to fit the data. The open symbols show the total electron capture cross section from the charge spectrometer experiment of Macdonald et al. (1972) for fluorine-nitrogen collisions. The dashed curve is our fit to these data,

again using the Nikolaev (1967) formalism but with a sum over all $n \geq 1$, and the same normalizing factor of 0.1. It is encouraging that with a single normalizing factor we could account for all of the data in Figure 3 with accuracy better than a factor of 2. In addition, the normalizing factor of 0.1 is within the range of the Nikolaev semiempirical normalizations for charge exchange on fast protons.

We also compared the predictions of the Schiff (1954) formula with the data shown in Figure 2. While for the H target, the formula gives an acceptable fit with the same normalization of 0.1, it predicts incorrect spectral dependencies for targets heavier than He, which is not surprising since the formula was developed for H-like targets in the ground state.

4.1.2. *Excitation cross section*

The plane-wave-Born-approximation (PWBA) gives a satisfactory description for the Coulomb excitation of atomic electrons (Bates 1962). Figure 3 shows a comparison of theoretical cross sections with the experimental data of Hopkins, Little, & Cue (1976a) for the excitation of $1s$ electrons which leads to K X-ray emission. The theoretical curves consist of the sum of the $1s \rightarrow 2p$ and $1s \rightarrow 3p$ excitation cross sections, excitations to higher levels, which have much smaller cross sections, being neglected. The cross sections for the excitation of F^{7+} are greater than twice those of F^{8+} (F^{7+} has two K-shell electrons which could be excited), because we took into account the screening of the nuclear charge of the projectile by the other K-shell electron. Although the PWBA theory indicates that the excitation cross sections scale as the target charge squared, the Hopkins et al. (1976a) measurements show that the cross sections for excitation by He are $\sim 20\%$ lower than four times the corresponding ones for excitation by H. This discrepancy was attributed to the screening effect of the helium electrons (Hopkins et al. 1976a). To take this effect into account, we used a normalization factor of 0.8 for all the target elements heavier than hydrogen in addition to the scaling with the target charge squared. This approximation has only a small impact on the final result, since the contribution of the elements heavier than He to the excitation represents less than 4% of the final X-ray production. We neglected the contributions of excitation reactions in which both the projectile and the target are excited based on the results of Moiseiwitsch & Stewart (1954).

4.1.3. *Equilibrium charge fractions*

The O ions lose energy more slowly than they capture and lose electrons by interacting with a neutral ambient medium of solar composition (see the discussion of Bussard et al. 1978 for fast Fe ions). Thus, in a steady state, the charge fractions F_n , where n is the number of bound electrons of the projectile, satisfy the equation

$$F_n \sigma_c^{(n)} = F_{n+1} \sigma_I^{(n+1)} , \quad (4)$$

where $\sigma_c^{(n)}$ and $\sigma_I^{(n)}$ are, respectively, the electron capture and ionization cross sections for O ions with n electrons interacting with an ambient medium of solar composition. Ionization cross sections scale approximately as the target charge squared (Rule 1977). Thus, because of the low abundances of the heavier elements (Anders & Grevesse 1989), the fast ions lose their electrons by colliding mainly with ambient H and He. This is not the case for electron captures because of the strong dependence of the charge exchange cross section on the charge of the target nucleus (e.g. Figure 2). We took into account the ambient H, He, C, N, O, Ne, Mg, Si, S and Fe to calculate the total electron capture of the fast O ions in the medium of solar composition. Ionization cross sections of O ions in collisions with neutral H and He were taken respectively from Watson (1976) and Rule (1977). The electron capture and loss cross sections for fast O in a medium of solar composition are shown in Figure 4a and the F_0 , F_1 and F_2 charge fractions determined from equation (4) are shown in Figure 4b. We see that contrary to the charge exchange cross sections, the ionization cross sections have a weak energy dependence. As most of the X-ray line emission is produced near the energy at which the charge exchange and ionization cross sections are equal, and because of the weak energy dependence of the ionization cross sections, the final X-ray line production is not very sensitive to the exact magnitude of the charge exchange cross section. We found that an uncertainty of a factor of 2 in the charge exchange cross section (§4.1.1) leads to only a 25% uncertainty in the X-ray emissivity.

4.1.4. K X-ray multiplicities

The multiplicities of the H-like (O VIII) and He-like (O VII) $K\alpha$ lines produced by a fast O of initial energy E_{n0} slowing down in a medium with solar abundances due to interactions with the ambient constituent j of abundance n_j/n_H can be obtained from equation (1),

$$M_{\text{O VIII}}(j) = \frac{A_i}{(1 + 1.8 \frac{n_{He}}{n_H})m_p} \left(\frac{n_j}{n_H} \right) \int_0^{E_{n0}} \frac{dE_n}{Z_i^2(ef f) \left(\frac{dE}{dx} \right)_{p,H}} \left(F_0 \sigma_{c;j}^{(0)}(2p) + F_1 \sigma_{ex;j}^{(1)}(1s \rightarrow 2p) \right) \quad (5)$$

and

$$M_{\text{O VII}}(j) = \frac{A_i}{(1 + 1.8 \frac{n_{He}}{n_H})m_p} \left(\frac{n_j}{n_H} \right) \int_0^{E_{n0}} \frac{dE_n}{Z_i^2(ef f) \left(\frac{dE}{dx} \right)_{p,H}} \left(F_1 \sigma_{c;j}^{(1)}(2p) + F_2 \sigma_{ex;j}^{(2)}(1s \rightarrow 2p) \right) . \quad (6)$$

Here the F_n are the charge fractions of the O ions; $\sigma_{c;j}^{(n)}(2p)$ is the electron capture cross section into the $2p$ level, either directly or following a cascade, by an ion which already has n electrons from the target element j ; $\sigma_{ex;j}^{(n)}(1s \rightarrow 2p)$ is the $1s \rightarrow 2p$ excitation cross section for an O ion having n electrons by the target element j . The O $K\beta$ X-ray multiplicities are obtained by replacing $2p$ by $3p$ in equations (5) and (6).

To calculate $\sigma_{c;j}^{(n)}(2p)$ and $\sigma_{c;j}^{(n)}(3p)$, we first calculated the total K X-ray production as in § 4.1.1, and then used the experimental result of Hopkins et al. (1974) to determine the relative contributions of the $K\alpha$ and the $K\beta$ lines. Hopkins et al. (1974) measured the K X-ray production

from fully stripped O of 1.9 MeV/nucleon interacting with various targets. As the projectiles were initially devoid of electrons, the detected K X-ray emission could have arisen only from electron capture. They found that, independent of the target charge, about 60% of the total K X-ray production was in the $K\alpha$ line and 20% in the $K\beta$ line, the remaining 20% coming from the rest of the series. Combining this result with the calculation of $\sigma_{ex;j}^{(n)}(1s \rightarrow 2p)$ and $\sigma_{ex;j}^{(n)}(1s \rightarrow 3p)$, we eventually found that each of the two $K\beta$ lines, i.e. from the H- and He-like O, represents 1/4 of the corresponding $K\alpha$ line.

We have evaluated equations (5) and (6) and the results are given in Tables 1 and 2, where we have separated the contributions from electron captures and excitations of $1s$ electrons. The multiplicities are independent of the initial O energy for $E_{n0} \gtrsim 10$ MeV/nucleon, because at these high values of E_{n0} the nuclei are fully stripped and the probability for capturing electrons is very small. The results of Tables 1 and 2 can be compared with the multiplicities given by Pravdo & Boldt (1975). Although our results for the contribution of charge exchange are ~ 4 times lower than theirs, the total $K\alpha$ X-ray production is only 1.8 times lower. This is because excitation is now seen to be the dominant mechanism. This result is supported by the accelerator measurement of Hopkins et al. (1976a), which provides a clear signature that excitation is the dominant process of K X-ray production for 1-3 MeV/nucleon F^{7+} and F^{8+} projectiles in hydrogen and helium. The same conclusion was found also by Bussard et al. (1978) for the $K\alpha$ X-ray emission from fast Fe. In particular, we can see from Table 2 that the excitation contribution to the O VII line production, which was not taken into account by Pravdo & Boldt (1975), represents 60% of the total multiplicity.

Using Equations (5) and (6) we can also evaluate the differential multiplicities $\sum_j dM_{O\text{ VIII}}(j)/dE_{n0}$ and $\sum_j dM_{O\text{ VII}}(j)/dE_{n0}$, i.e. the number of photons produced by the projectile, due to interactions with all the constituents of the ambient medium, as it slows down over the differential energy interval dE_n . The results for O are shown in Table 3 and Figure 5c. Similar multiplicities for C, N, Ne, Mg, Si, S and Fe are also shown in Tables 3 and 4 and in Figures 5 and 6. These multiplicities are discussed below. We see that for O the differential multiplicities peak around 1 MeV/nucleon and fall off rapidly at both lower and higher energies. The differential multiplicities for O can be compared with the results of Pravdo & Boldt (1975). The positions of the peaks are consistent although, as already discussed, the magnitudes of the multiplicities are lower.

4.2. K X-rays from the other fast ions

The major X-ray lines from the fast ions are given in Table 5. We used the same formalisms for the charge exchange and the excitation cross sections as described for O. In particular, we used for the charge exchange cross sections the same normalization factor of 0.1 for all the projectiles and targets (§ 4.1.1). We checked our charge exchange calculations with the experimental data of Berkner et al. (1977) for 3.4 MeV/nucleon Fe projectiles in charge states +20 to +25 interacting

with H_2 and found agreement within 40%. For the ionization cross sections, we used the scaling relation (Rule 1977)

$$\sigma_I^{Z_i}(v_i) = (8/Z_i)^4 \sigma_I^8(8v_i/Z_i) , \quad (7)$$

where v_i and Z_i are the speed and charge of the projectile, and σ_I^8 is the ionization cross section of fast O ions in an ambient medium of solar composition (§4.1.3, and Figure 4a). We assumed for all the fast ions that the $\text{K}\alpha$ and the $\text{K}\beta$ lines represent respectively 60% and 20% of the K X-ray production from electron capture.

The results for the $\text{K}\alpha$ differential multiplicities, along with the total multiplicities, are shown in Figures 5 and 6. As for O, we found that the multiplicities for the $\text{K}\beta$ photons are approximately 1/4 of the corresponding $\text{K}\alpha$ multiplicities. The multiplicities decrease with increasing projectile charge, from a total multiplicity of 87 photons/projectile for C to 7 photons/projectile for Fe. The projectile energies at which the differential multiplicities peak increase with increasing projectile charge. Our results for Fe are in good agreement with the previous calculations of Bussard et al. (1978). In particular, we agree that excitation of $1s$ electrons is the dominant mechanism of $\text{K}\alpha$ X-ray production, that ambient O and Fe are the main contributors to electron capture by fast Fe ions and that the peak of the X-ray line production from fast Fe is at ~ 9 MeV/nucleon. Both calculations of the total emissivity of Fe $\text{K}\alpha$ lines agree within 20% (see the table 2 and the notes added in the manuscript of Bussard et al. 1978).

4.3. K X-rays from the ambient atoms

The K X-ray line emission from the ambient atoms results from the filling of inner-shell vacancies produced by the fast ions. In the case of proton impact, the line energies correspond to the difference of the orbital energies, because both the vacancy production and the subsequent filling of the vacancy occur in times short compared to the relaxation times for the atomic wave functions (Garcia et al. 1973). For heavy-ion collisions, the lines could be shifted by several tens of eV, significantly broadened and slitted up into several components, due to multiple inner-shell plus outer-shell simultaneous ionizations (Garcia et al. 1973). We have not taken into account these effects, although we believe that they could provide interesting constraints on the accelerated particle composition through fine spectroscopy. We considered the $\text{K}\alpha$ and $\text{K}\beta$ lines from ambient C, N, O, Ne, Mg, Si, S, Ar, S and Fe and have determined the transition energies (Table 6) from the atomic electron binding energy tables of Sevier (1979). We do not consider $\text{K}\beta$ X-rays from C, N, O, Ne and Mg, as these atoms in their ground state do not have $3p$ electrons.

The X-ray line production cross section can be written as

$$\sigma_X = \sigma_I w k, \quad (8)$$

where σ_I is the cross section for the collisional ionization leading to the K-shell vacancy, w is the fluorescence yield for the K shell (Krause 1979) and k is the relative line intensity among the

possible transitions which can fill the inner-shell vacancy (Salem, Panossian, & Krause 1974). For proton impact, we calculated the ionization cross sections from the semiempirical formula of Johansson & Johansson (1976), with an extrapolation at high energy from appendix 2 of Garcia et al. (1973). For heavier projectiles, we assumed a Z_i^2 dependence, as predicted by both the PWBA and the impulse approximation theories. This assumption gives a poor description of the available experimental data at low energies due to molecular effects, but becomes reasonable as the cross section reaches its maximum, i.e. for $E_n \simeq (m_p/m_e)u_K$ (in MeV/nucleon), where u_K is the binding energy of the K shell (Garcia et al. 1973).

K X-ray production cross sections for fast protons colliding with C, O, Si and Fe are shown in Figure 7. The $K\alpha$ line production cross sections do not show a strong dependence on the target charge even though the ionization cross section varies as Z_j^{-4} (Johansson & Johansson 1976), because this variation is partially compensated by the $Z_j^{3.25}$ dependence of the fluorescence yields up to Fe (Krause 1979).

5. Results and Applications for Orion

We developed a code for the calculation of the X-ray emission resulting from the various continuum and line producing processes discussed above. The code allows the use of various accelerated particle energy spectra and compositions in a steady state, thick target model. The ambient medium is assumed to be neutral with a solar composition. We discuss in § 5.1 the modifications that would result for X-ray production in a partially ionized medium and in §5.2 those for a time-dependent model. We took into account the photoelectric absorption of the X-rays, again using solar abundances, and the cross sections of Morrison & McCammon (1983). We present results normalized to the accompanying 3-7 MeV nuclear gamma-ray line emission which we calculated as in Ramaty et al. (1996).

The calculated X-ray fluxes, normalized to a 3-7 MeV nuclear gamma-ray flux of 10^{-4} photons $\text{cm}^{-2} \text{s}^{-1}$ (the approximate value of the observed gamma-ray line emission from Orion), are shown in Figures 8 and 9 for the CRS and WC compositions, respectively. We took into account photoelectric absorption using $N_H = 3 \times 10^{21} \text{ cm}^{-2}$, our estimate for the H column density towards Orion. We estimated this column density from the HI survey of Heiles & Habing (1974) and the CO map of Dame et al. (1987), together with a CO-to- H_2 conversion factor of $(1.06 \pm 0.14) \times 10^{20} \text{ cm}^{-2} (\text{K km s}^{-1})^{-1}$ (Digel et al. 1995).

We first note that the continuum emission is indeed dominated by the inverse bremsstrahlung (§ 3). We have calculated the SEB differential luminosity for $E_0 = 30 \text{ MeV/nucleon}$ without including the photoelectric absorption and compared the results with those given in figure 1 of Dogiel et al. (1997). For the CRS composition our results are lower than theirs by factors of 19, 6.6 and 1.9 at $E_x = 0.2, 1$ and 10 keV , respectively; for the WC composition, the discrepancy is even larger, the corresponding factors being 75, 31 and 9. The discrepancy is due, in part, to the

approximate normalization to the nuclear gamma-ray line emission used by Dogiel et al. (1997). However, by repeating their calculation using the same formalism and input data (Hayakawa 1969), we find results which agree with our more accurate approach but which are lower than that of Dogiel et al. (1997) by about an order of magnitude at 1 keV.

We calculated the width of the lines produced by the fast ions assuming an isotropic angular distribution for these particles. We see that below about 1 keV the X-ray emission is dominated by these lines, in particular the lines from fast C and O. For the much narrower lines from the ambient atoms, we assumed delta functions at the nominal line energies (Table 6) and plotted the spectra in 10 eV bins. The most prominent narrow line is that at 6.4 keV from ambient Fe. The width of the lines resulting from de-excitations in the fast ions are quite broad. For example, the O lines, which are produced around 1 MeV/nucleon, have widths of about 0.06 keV (FWHM). This large width distinguishes them from the X-ray lines produced in a hot plasma.

By comparing Figures 8 and 9, we see that the line-to-continuum ratio below 1 keV is lower for the CRS composition than for the WC composition because of the additional bremsstrahlung from the protons and α -particles. The line-to-continuum ratio below 1 keV is also lower for the higher E_0 , because the fast ions produce line emission only at the low energies (Figures 5 and 6). The X-ray emission at high energies ($\gtrsim 10$ keV) is very sensitive to the value of E_0 .

In Figures 10 and 11 we compare the expected X-ray fluxes from Orion with the diffuse extragalactic X-ray background. We calculate the X-ray emission for the CRS composition with $E_0=100$ MeV/nucleon and for the WC composition with $E_0=20$ MeV/nucleon. We consider two cases: uniform gamma-ray emission from the box $[201^\circ \leq l^{II} \leq 217.5^\circ, -21^\circ \leq b^{II} \leq -9^\circ]$ which contains almost all of the 3-7 MeV emission observed with COMPTEL, $(12.8 \pm 1.5) \times 10^{-5}$ photons $\text{cm}^{-2} \text{s}^{-1}$ (Bloemen et al. 1997); the hot spot observed with COMPTEL at $l^{II}=213.6^\circ, b^{II}=-15.7^\circ$ from which the 3-7 MeV emission flux is $(3.3 \pm 0.8) \times 10^{-5}$ photons $\text{cm}^{-2} \text{s}^{-1}$ (H. Bloemen, private communication, 1996). As the size of the spot is not well known, we considered a 9 degree² box $[212.25^\circ \leq l^{II} \leq 215.25^\circ, -17.25^\circ \leq b^{II} \leq -14.25^\circ]$ which represents the approximate extent of the hot spot in the published COMPTEL map (Bloemen et al. 1997). We took the extragalactic diffuse X-ray background from Gendreau et al. (1995) below 10 keV and from Gruber (1992) at higher energies. We increased the Gruber (1992) data by 9% to achieve a smooth transition to the Gendreau et al. (1995) data.

Considering first the X-ray continuum at high energies, we see that if the gamma-ray source is uniformly spread over the entire 200 degree² box (Figures 10a and 11a), it will be very difficult to observe these X-rays because the predicted emission is much lower than the extragalactic background. In the case of the 9 degree² hot spot, the chances of detecting the high energy X-ray continuum above the extragalactic background are better, in particular for the CRS composition with $E_0=100$ MeV/nucleon (Figure 10b) which yields the highest X-ray continuum for a given nuclear gamma-ray flux. On the other hand, the predicted line emission, in particular the lines from fast O, exceeds the extragalactic background independent of the spectrum and composition

of the accelerated particles.

ROSAT observations can be used to test our predictions of the expected line emission below 2 keV. We used the ROSAT all-sky survey (Snowden et al. 1995) to compare our calculations with the observed count rate in the ROSAT R45 energy band, i.e. from 0.47 to 1.2 keV (Snowden et al. 1994). We considered the same two source regions as in Figures 10 and 11: the 200 degree² box for which we assume a uniform gamma-ray emission; and the 9 degree² gamma-ray hot spot. For the 200 degree² box ROSAT/PSPC detected a total of 70.1 counts s⁻¹ in the R45 band. We subtracted the contributions of the Orion nebula region and the Ori OB1 association, which were interpreted as thermal emission most likely from T Tauri type stars (Yamauchi, Koyama, & Inda-Koide 1994; Yamauchi et al. 1996). The remaining count rate of 60.6 counts s⁻¹ is plotted in Figure 12a. For the 9 degree² hot spot there are 2.7 counts s⁻¹ in the ROSAT/PSPC R45 band (Figure 12b).

In the 200 degree² box, the corresponding X-ray luminosity is $\sim 2 \times 10^{34}$ ergs s⁻¹ assuming a distance to Orion of 450 pc. This luminosity is 20 times greater than the upper limit derived by Dogiel et al. (1997), even though our value pertains to the 0.47-1.2 keV range whereas that of Dogiel et al. (1997) is for X-rays between 0.5 and 2 keV. We believe that the discrepancy is due to the fact that Dogiel et al. (1997) searched for only nonthermal continuum whereas we considered all the emission that could not be related to known sources in Orion (see above). In particular, because of the presence of the lines (Figures 8 and 9), the total X-ray emission from low energy particle interactions may look similar to thermal emission (Raymond & Smith 1977) given the rather poor energy resolution of ROSAT/PSPC.

Also shown in Figure 12 are the predicted R45 count rates obtained by convoluting the calculated X-ray spectra with the ROSAT/PSPC response function (Snowden et al. 1994) and taking into account photoelectric absorption with the same H column density of 3×10^{21} cm⁻² for the two source regions. The results, normalized to the gamma-ray intensities, are given as functions of the characteristic energy E_0 [Eq. (2)] for the CRS, OB and WC compositions. The count rates due to extragalactic background were obtained in the same manner, i.e. by convoluting the spectrum given by Gendreau et al. (1995) with the ROSAT/PSPC response function and using the same H column density for the photoelectric absorption as for the two Orion source regions.

In Figure 12 the increase of the predicted count rates as the accelerated particle spectrum becomes softer (i.e. with decreasing E_0) is due to the decrease of the gamma-ray production relative to the X-ray production, which occurs at much lower energies than the gamma-ray production. The CRS composition provides the lowest X-ray emission because of its highest proton and α -particle abundances relative to those of ¹²C and ¹⁶O. Indeed, accelerated protons and α -particles produce 3-7 MeV emission while interacting with ambient CNO, but no significant X-ray line emission in the ROSAT energy range. We note that the extragalactic X-ray background accounts for only 1/6 of the observed count rates in both Figures 12a and 12b. We see in Figure 12a that except for the very low E_0 , the calculated count rates are lower than the observed

rate, suggesting a contribution of other sources, for example T Tauri stars. On the other hand, we see in Figure 12b that the predicted X-ray counterpart of the observed nuclear gamma-ray line emission from the 9 degree² hot spot exceeds the ROSAT count rate except at the highest allowed values of E_0 near 100 MeV/nucleon. This discrepancy could be mitigated by assuming that the area of the gamma-ray hot spot is larger than 9 degree², although for a smaller area a more severe discrepancy would ensue. The discrepancy could be resolved if the X-rays and gamma rays are produced by accelerated particles interacting in a partially ionized medium, for example at cloud boundaries (Bykov & Bloemen 1994; Ramaty et al. 1997a,b; Kozlovsky et al. 1997; Parizot et al. 1997a), or in a time-dependent model in which the spectrum of the accelerated particles has become quite flat because of energy losses. We elaborate on these two effects in the next two subsections.

5.1. Modifications due to a partially ionized ambient medium

We consider the effects of a partially ionized ambient medium on the K X-ray production in the ROSAT R45 energy band (0.47 to 1.2 keV). In this energy range, the K X-rays are produced by fast C, N, O and Ne. As the nature of the cosmic ray ionization at the cloud boundaries is not well understood, we assume for simplicity that the ambient H and He are fully ionized but that the heavier ambient elements remain essentially neutral. Thus the fast ions capture electrons from ambient C and heavier atoms only. As the capture cross sections increase rapidly toward lower energies while the electron loss cross sections are essentially constant (Figure 4a), the charge state distribution of the fast ions in an ionized medium is quite similar to that in a neutral medium (Figure 4b), except that it is established at lower values of E_n . Consequently, K X-rays are also produced at lower energies (about 0.1-1 MeV/nucleon for the C, N, O and Ne K X-rays) in an ionized medium than in a neutral medium. Although the fast ions do not capture electrons from ambient H and He, the rate of electron capture is not very different from that in a neutral medium because of the more efficient electron capture from heavier ambient atoms caused by the increase of the capture cross sections toward lower energies (Figure 4a). We also do not expect substantial reductions of the magnitude of the K X-ray multiplicities due to excitation, because the excitations are mainly due to the ambient nuclei and the cross sections are only slowly decreasing at lower energies (Figure 3).

The main difference between K X-ray production from fast ions interacting in an ionized or a neutral medium is due to the energy losses. It is well-known that fast ions lose more energy in a plasma than in a neutral medium, because the collective long-range Coulomb interactions are more efficient than ionization. Both the X-ray and gamma-ray production rates are reduced, but as we shall see, the effect is stronger for the X-rays.

The energy loss rate depends on the effective charge of the fast ion. We calculated the effective charge of a fast O in a medium of solar composition in which H and He are fully ionized and the result is shown by the dashed curve in Figure 13a. We found that this effective charge

could be approximated by a formula similar to that used to describe the effective charge in a neutral medium (§2),

$$Z_i(ef\!f) = Z_i[1 - \exp(-220\beta_i/Z_i^{2/3})], \quad (9)$$

with a modified exponential to take into account the increase of the fast ion charge in the ionized medium. We then calculated the O ion energy loss in a plasma using equations (4.21) and (4.22) from Mannheim and Schlickeiser (1994), in which we substituted the nuclear charge of the projectile by its effective charge [Eq. (9)]. We assumed a typical temperature of 10^4 K at cloud boundaries. The energy loss is not very sensitive to temperature for $E_n \geq 0.1$ MeV/nucleon. In Figure 13b we show the ratio of the energy loss in an ionized medium to that in a neutral medium for fast O ions. We see that while at high energies the increase in the energy loss rate is about a factor of 2, below an MeV/nucleon the energy loss rate in an ionized medium exceeds that in a neutral medium by more than a factor of 6. This result is supported by the laboratory measurements of Hoffmann et al. (1994) for the energy loss of various fast ions in a hydrogen plasma.

Because the X-ray line emission is produced between about 0.1 and 1 MeV/nucleon, while the 3-7 MeV gamma-ray line production occurs essentially above 10 MeV/nucleon (Ramaty et al. 1996), the ratio of thick target [Eq. (1)] X-ray to gamma-ray line production in an ionized medium will be lower than in a neutral medium, by about a factor of 3. We emphasize that this decrease is mainly due to the increase in the fast ion energy loss rate rather than the changes in the electron capture, ionization and excitation.

5.2. Modifications due to a time-dependent accelerated particle population

Because the K X-ray production in the ROSAT R45 energy band (0.47 to 1.2 keV) is due to very low energy ions, time-dependent effects could significantly reduce the number of such ions relative to that of the higher energy gamma-ray line producing ions, thereby decreasing the X-ray production rate relative to the gamma-ray production rate.

To illustrate the effect, we first calculate the differential equilibrium particle number $Y(E)$ for steady state, thick target interactions. This is given by (see Eq. 1)

$$Y(E) = \left(\frac{dE}{dt}\right)^{-1} \int_E^\infty \frac{dN}{dt}(E')dE' . \quad (10)$$

where the energy loss rate in a neutral medium is

$$\left(\frac{dE}{dt}\right) = (1 + 1.8 \frac{n_{He}}{n_H}) m_p n_H v \frac{Z^2(ef\!f)}{A} \left(\frac{dE}{dx}\right)_{p,H} . \quad (11)$$

The dashed curve in Figure 14 shows this $Y(E)$ for O ions with $E_0=30$ MeV/nucleon, normalized such that the instantaneous energy deposition rate, $16 \int_0^\infty Y(E)(dE/dt)dE$, is 10^{38} erg/s for an

average ambient hydrogen density of 10 cm^{-3} . This is the approximate energy deposition rate that accompanies the gamma-ray production rate in Orion due to O ions (Ramaty et al. 1996). While the energy deposition rate can be calculated independent of the ambient density, the equilibrium number does depend on the density which is quite uncertain. The value of 10 cm^{-3} is not unreasonable if the accelerated particles spend part of their life time in the clouds.

Next we assume that the accelerated particles are injected as a delta function in time (i.e. over a time interval which is very short compared to the life time against energy losses). The time-dependent differential particle number is then given by (e.g. Parizot et al. 1997b)

$$Y(E, t) = \frac{dE'/dt}{dE/dt} Q(E') . \quad (12)$$

Here

$$t = \int_E^{E'} \left[\frac{dE}{dt}(E'') \right]^{-1} dE'' \quad (13)$$

is the elapsed time since the injection of the particles and the energy loss rates in equation (12) are derived at E' and E . We normalize the injection source $Q(E)$ such that the total energy deposited at $t=0$ in the time-dependent case equals the deposited steady state energy over a time period of 10^5 years. This leads to a total deposited energy in O nuclei of 3.2×10^{50} ergs. This value, together with the contributions of the other accelerated nuclei, yields a total accelerated particle energy content of about 10^{51} ergs (depending on the assumed composition), which could have been supplied by the supernova that is thought to have occurred about 80,000 years ago and reheated the Orion-Eridanus bubble (Burrows et al. 1993).

The results are shown by the solid curves in Figure 14 for the same ambient density and E_0 as used for the steady state result. We see that, as time progresses, the differential number densities at low energies are suppressed relative to those at higher energies. Since in a neutral medium the K X-ray line emission from O is typically produced around 1 MeV/nucleon while the gamma rays are produced above 10 MeV/nucleon, we expect a significant reduction of the X-ray line to gamma-ray line production ratio relative to the corresponding production ratio for the steady state case. At $t=3 \times 10^4$ years, for example, the reduction is about an order of magnitude.

6. Conclusions

We have investigated all the processes that lead to X-ray production by low energy cosmic rays for a variety of accelerated particle compositions and energy spectra. We demonstrated that the dominant continuum producing process is inverse bremsstrahlung produced by fast ions interacting with ambient electrons. In addition, there is also a significant contribution from the bremsstrahlung produced by secondary knock-on electrons. However, below a few keV the total X-ray emission produced by accelerated ions is dominated by relatively broad line emission (line

widths $\delta E/E \simeq 0.1$) resulting from de-excitations in the fast ions following electron captures and excitations. In addition, accelerated particle interactions also produce much narrower X-ray lines, due to inner-shell vacancy creation. The most prominent of such line is that at 6.4 keV from ambient Fe.

We have calculated the X-ray line and continuum emission produced by the accelerated particles in Orion which are thought to be responsible for the nuclear gamma-ray line emission observed with COMPTEL (Bloemen et al. 1994, 1997). By first comparing the results with the extragalactic diffuse X-ray background, we found that while the continuum is generally below this background, the line emission from about 0.5 to 1.5 keV exceeds the background for all the combination of parameters that we considered. We wish to point out that there could be a significant contribution to the ~ 0.5 -1.5 keV diffuse X-ray background from as-yet unknown sources within our Galaxy (e.g. Park et al. 1997), leaving the possibility that a substantial fraction of the observed X-ray intensity in this energy range results from low energy cosmic ray interactions.

We have also compared our results with ROSAT observations of Orion in the 0.47 to 1.2 keV energy band, again normalizing the X-ray emission to the observed gamma-ray emission. We found that there is no conflict between the predicted total X-ray emission (lines and continuum) and the data for a broad range of parameters if the gamma-ray line emission is uniformly distributed over the entire molecular cloud complex. This conclusion differs from our previous one (Ramaty et al. 1997a) because of a lower predicted X-ray line emission, resulting from improved atomic physics input, and because our estimated ROSAT flux from Orion is higher than the upper limit given by Dogiel et al. (1997). However, the COMPTEL data show significant spatial structure. We found that for the most prominent hot spot in the COMPTEL map, the standard thick target, steady state interaction model, with a neutral ambient medium, predicts X-ray fluxes which exceed the ROSAT data for a broad range of parameters. But the calculations could be consistent with the data for any one, or a combination of the following possibilities: a very hard accelerated particle spectrum; a partially ionized ambient medium; and a time-dependent accelerated particle energy spectrum resulting from essentially instantaneous acceleration some tens of thousand of years ago.

There are as-yet no astrophysical X-ray observations that would unambiguously indicate an origin resulting from low energy, accelerated ion interactions. Our calculations show that the most promising signatures are the relatively broad lines between 0.5 and 1.5 keV, mainly the lines from fast O, and that a promising target is the Orion region where the presence of such accelerated particles is known from gamma-ray line observations.

We acknowledge K. Omidvar for discussions on the atomic processes leading to X-ray line production. V. T. acknowledges an NRC-NASA/GSFC Research Associateship.

REFERENCES

- Anders, E., & Grevesse, N. 1989, *Geochim. Cosmochim. Acta*, 53, 197
- Anholt, R. 1985, *Rev. Mod. Phys.*, 57, 995
- Bates, D. R. 1962, *Atomic and Molecular Processes* (New York: Academic Press)
- Belkić, Dž., Gayet, R., & Salin, A. 1979, *Phys. Rept.*, 56, 279
- Berger, M. J., & Seltzer, S. M. 1982, *Stopping Powers and Ranges of Electrons and Positrons*, National Bureau of Standards report: NBSIR 82-2550, U.S. Dept. of Commerce, Washington, D.C. 20234
- Berkner, K. H., Graham, W. G., Pyle, R. V., Schlachter, A. S., & Stearns, J. W. 1977, *Phys. Lett.*, 62A, 407
- Bloemen, H., et al. 1994, *A&A*, 281, L5
- Bloemen, H., et al. 1997, *ApJ*, 475, L25
- Boldt, E. A., & Serlemitsos, P. 1969, *ApJ*, 157, 557
- Burrows, D. N., Singh, K. P., Nousek, J. A., Garmire, G. P., & Good, J. 1993, *ApJ*, 406, 97
- Bussard, R. W., Ramaty, R., & Omidvar, K. 1978, *ApJ*, 220, 353
- Bykov, A. M., & Fleishman, G. D. 1992, *MNRAS*, 255, 269
- Bykov, A. M., & Bloemen, H. 1994, *A&A*, 283, L1
- Bykov, A. M. 1995, *Space Sci. Rev.*, 74, 397
- Cahill, T. A. 1980, *Ann. Rev. Nucl. Part. Sci.*, 30, 211
- Cassé, M., Lehoucq, R., & Vangioni-Flam, E. 1995, *Nature*, 373, 318
- Chu, T. C., et al. 1981, *Phys. Rev. A*, 24, 1720
- Cowsik, R., & Friedlander, M. 1995, *ApJ*, 444, L29
- Dame, T. M., et al. 1987, *ApJ*, 305, 892
- Digel, S. W., Hunter, S. D., & Mukherjee, R. 1995, *ApJ*, 441, 270
- Dogiel, V. A., Freyberg, M. J., Morfill, G. E., & Schönfelder, V. 1997, *25th International Cosmic Ray Conference*, ed. M. S. Potgieter et al., vol. 3, 133
- Ellison, D. C., & Ramaty, R. 1985, *ApJ*, 298, 400

- Ferguson, S. M., Macdonald, J. R., Chiao, T., Ellsworth, L. D., & Savoy, S. A. 1973, *Phys. Rev. A*, 8, 2417
- Garcia, J. D., Fortner, R. J., & Kavanagh, T. M. 1973, *Rev. Mod. Phys.*, 45, 111
- Gendreau, K. C., et al. 1995, *Publ. Astron. Soc. Japan*, 47, L5
- Gruber, D. E. 1992, in *X-ray background*, eds. X Barcons and A. C. Fabian (Cambridge University Press), 44
- Guffey, J. A., Ellsworth, L. D., & Macdonald, J. R. 1977, *Phys. Rev. A*, 15, 1863
- Harris, M. J., et al. 1998, *A&A*, 329, 624
- Hayakawa, S., Matsuoka, M. 1964, *Suppl. of the Progress of Theoretical Physics*, 30, 204
- Hayakawa, S. 1969, *Cosmic Ray Physics, Nuclear and Astrophysical Aspects* (New York, Wiley)
- Hoffmann, D. H. H., et al. 1994, *Nuclear Instruments and Methods in Physics Research B*, 90, 1
- Heiles, C., & Habing, H. J. 1974, *A&AS*, 14, 1
- Hopkins, F., Kauffman, R. L., Woods, C. W., & Richard, P. 1974, *Phys. Rev. A*, 9, 2413
- Hopkins, F., Little, A., & Cue, N. 1976a, *Phys. Rev. A*, 14, 1634
- Hopkins, F., et al. 1976b, *Phys. Rev. A*, 13, 74
- Ip, W.-H. 1995, *A&A*, 300, 283
- Johansson, S. A. E., & Johansson, T. B. 1976, *Nucl. Inst. Meth.*, 137, 473
- Kelly, R. L. 1987, *J. Phys. Chem. Ref. Data*, 16, Suppl. 1
- Koch, H. W., & Motz, J. W. 1959, *Rev. Mod. Phys.*, 31, 920
- Kozlovsky, B., Ramaty, R., & Lingenfelter, R. E. 1997, *ApJ*, 484, 286
- Krause, M. O. 1979, *J. Phys. Chem. Ref. Data*, 8, 307
- Macdonald, J. R., Fergusson, S. M., Chiao, T., Ellsworth, L. D., & Savoy, S. A. 1972, *Phys. Rev. A*, 5, 1188
- Mannheim, K., & Schlickeiser, R. 1994, *A&A*, 286, 983
- Matthews, D., Braithwaite, W. J., Wolter, H. H., & Moore, C. F. 1973, *Phys. Rev. A*, 8, 1397
- Moiseiwitsch, B. L., & Stewart, A. L. 1954, *Proc. Phys. Soc. A*, 67, 74
- Morrison, R., & McCammon, D. 1983, *ApJ*, 270, 119

- Murphy, R. J., et al. 1996, *ApJ*, 473, 990
- Nath, B. B., & Biermann, P. L. 1994, *MNRAS*, 270, L33
- Nikolaev, V. S. 1967, *Soviet Phys.-JETP*, 24, 847
- Parizot, E. M. G., Cassé, M., & Vangioni-Flam, E. 1997a, *A&A*, 328, 107
- Parizot, E. M. G., Lehoucq, R., Cassé, M., & Vangioni-Flam, E. 1997b, in *Proc. 2nd INTEGRAL Workshop*, ed. C. Winkler et al. (ESA SP-382), 97
- Park, S., Finley, J. P., Snowden, S. L., & Dame, T. M. 1997, *ApJ*, 476, 177
- Pierce, T. E., & Blann, M. 1968, *Phys. Rev.*, 173, 390
- Pravdo, S. H., & Boldt, E. A. 1975, *ApJ*, 200, 727
- Ramaty, R. 1996, *A&AS*, 120, C373
- Ramaty, R., Kozlovsky, B., & Lingenfelter, R. E. 1995, *ApJ*, 438, L21
- Ramaty, R., Kozlovsky, B., & Lingenfelter, R. E. 1996, *ApJ*, 456, 525
- Ramaty, R., Kozlovsky, B., & Tatischeff, V. 1997a, *Proc. 4th Compton Symposium*, (AIP: New York), vol. 2, 1049
- Ramaty, R., Kozlovsky, B., & Lingenfelter, R. E. 1997b, in *Proc. 2nd INTEGRAL Workshop*, ed. C. Winkler et al. (ESA SP-382), 41
- Raymond, J. C., & Smith, B. W. 1977, *ApJS*, 35, 419
- Rudd, M. E., et al. 1966, *Phys. Rev.*, 151, 20
- Rule, D. W. 1977, *Phys. Rev. A*, 16, 19
- Salem, S. I., Panossian, S. L., & Krause, R. A. 1974, *Atomic Data and Nucl. Data Tables*, 14, 91
- Schiff, H. 1954, *Canadian J. Phys.*, 32, 393
- Sevier, K. D. 1979, *Atomic Data and Nucl. Data Tables*, 24, 323
- Silk, J., & Steigman, G. 1969, *Phys. Rev. Lett.*, 23, 597
- Slater, J. C. 1930, *Phys. Rev.*, 36, 57
- Snowden, S. L., McCammon, D., Burrows, D. N., & Mendenhall, J. A. 1994, *ApJ* 454, 643
- Snowden, S. L., et al. 1995, *ApJ* 454, 643

- Tatischeff, V., Ramaty, R., & Mandzhavidze, N. 1997, Proc. 4th Compton Symposium, (AIP: New York), vol.2, 1054
- Toburen, L. H., & Wilson, W. E. 1972, Phys. Rev. A, 5, 247
- Watson, W. D. 1976, ApJ, 206, 842
- Yamauchi, S., Koyama, K., & Inda-Koide, M. 1994, Publ. Astron. Soc. Japan, 46, 473
- Yamauchi, S., Koyama, K., Sakano, M., & Okada, K. 1996, Publ. Astron. Soc. Japan, 48, 719

Table 1. Multiplicity of O VIII line X-rays

Elements	Electron capture	Excitation	Totals
H	1.9	8.1	10.0
He	4.0	2.2	6.2
C	0.43	$7.1 \cdot 10^{-2}$	0.50
N	0.15	$3.1 \cdot 10^{-2}$	0.18
O	1.2	0.31	1.5
Ne	0.23	$7.3 \cdot 10^{-2}$	0.30
Mg	0.11	$3.4 \cdot 10^{-2}$	0.14
Si	0.14	$4.3 \cdot 10^{-2}$	0.18
S	$8.8 \cdot 10^{-2}$	$3.0 \cdot 10^{-2}$	0.12
Fe	0.21	0.14	0.35
Totals	8.5	11.0	19.5

Table 2. Multiplicity of O VII line X-rays

Elements	Electron capture	Excitation	Totals
H	4.1	12.4	16.5
He	6.8	3.4	10.3
C	0.24	0.11	0.34
N	$7.2 \cdot 10^{-2}$	$4.6 \cdot 10^{-2}$	0.12
O	0.59	0.47	1.1
Ne	0.14	0.11	0.25
Mg	$6.7 \cdot 10^{-2}$	$5.0 \cdot 10^{-2}$	0.12
Si	$7.6 \cdot 10^{-2}$	$6.4 \cdot 10^{-2}$	0.14
S	$4.1 \cdot 10^{-2}$	$4.4 \cdot 10^{-2}$	$8.5 \cdot 10^{-2}$
Fe	0.10	0.21	0.32
Totals	12.2	16.9	29.2

Table 3. Multiplicity of C, N, O and Ne $K\alpha$ lines

ΔE (MeV/nucleon)	C		N		O		Ne	
	H-like	He-like	H-like	He-like	H-like	He-like	H-like	He-like
0.1 - 0.2	0.25E-03	0.42E+00	-	0.23E-01	-	0.13E-02	-	-
0.2 - 0.3	0.19E-01	0.37E+01	0.54E-03	0.45E+00	-	0.44E-01	-	0.52E-03
0.3 - 0.4	0.21E+00	0.90E+01	0.12E-01	0.21E+01	0.56E-03	0.35E+00	-	0.73E-02
0.4 - 0.5	0.92E+00	0.12E+02	0.87E-01	0.45E+01	0.67E-02	0.12E+01	-	0.47E-01
0.5 - 0.6	0.22E+01	0.11E+02	0.33E+00	0.62E+01	0.37E-01	0.23E+01	0.33E-03	0.17E+00
0.6 - 0.7	0.35E+01	0.79E+01	0.80E+00	0.67E+01	0.12E+00	0.33E+01	0.20E-02	0.42E+00
0.7 - 0.8	0.42E+01	0.48E+01	0.14E+01	0.60E+01	0.30E+00	0.39E+01	0.77E-02	0.77E+00
0.8 - 0.9	0.41E+01	0.26E+01	0.20E+01	0.46E+01	0.56E+00	0.40E+01	0.22E-01	0.11E+01
0.9 - 1.0	0.35E+01	0.13E+01	0.24E+01	0.31E+01	0.88E+00	0.36E+01	0.51E-01	0.15E+01
1.0 - 1.5	0.88E+01	0.13E+01	0.96E+01	0.47E+01	0.68E+01	0.87E+01	0.13E+01	0.88E+01
1.5 - 2.0	0.26E+01	0.87E-01	0.40E+01	0.41E+00	0.48E+01	0.14E+01	0.33E+01	0.50E+01
2.0 - 2.5	0.10E+01	0.12E-01	0.17E+01	0.62E-01	0.24E+01	0.23E+00	0.31E+01	0.16E+01
2.5 - 3.0	0.50E+00	0.29E-02	0.84E+00	0.15E-01	0.12E+01	0.56E-01	0.21E+01	0.49E+00
3.0 - 3.5	0.28E+00	0.89E-03	0.47E+00	0.46E-02	0.72E+00	0.18E-01	0.14E+01	0.17E+00
3.5 - 4.0	0.17E+00	0.33E-03	0.29E+00	0.17E-02	0.45E+00	0.68E-02	0.90E+00	0.65E-01
4.0 - 4.5	0.11E+00	0.14E-03	0.19E+00	0.75E-03	0.30E+00	0.30E-02	0.62E+00	0.29E-01
4.5 - 5.0	0.74E-01	-	0.13E+00	0.35E-03	0.21E+00	0.14E-02	0.44E+00	0.14E-01
5.0 - 6.0	0.90E-01	-	0.16E+00	0.28E-03	0.26E+00	0.11E-02	0.56E+00	0.11E-01
6.0 - 7.0	0.49E-01	-	0.92E-01	-	0.15E+00	0.37E-03	0.33E+00	0.37E-02
7.0 - 8.0	0.29E-01	-	0.55E-01	-	0.91E-01	0.14E-03	0.21E+00	0.14E-02
8.0 - 9.0	0.18E-01	-	0.35E-01	-	0.59E-01	-	0.14E+00	0.62E-03
9.0 - 10.0	0.12E-01	-	0.23E-01	-	0.40E-01	-	0.94E-01	0.29E-03
10.0 - 12.0	0.13E-01	-	0.23E-01	-	0.41E-01	-	0.10E+00	0.16E-03
12.0 - 14.0	0.67E-02	-	0.13E-01	-	0.23E-01	-	0.59E-01	-
14.0 - 16.0	0.37E-02	-	0.78E-02	-	0.14E-01	-	0.37E-01	-
16.0 - 18.0	0.23E-02	-	0.50E-02	-	0.93E-02	-	0.25E-01	-
18.0 - 20.0	0.14E-02	-	0.33E-02	-	0.63E-02	-	0.17E-01	-
TOTALS	32.53	54.14	24.66	38.84	19.55	29.16	14.79	20.22

Table 4. Multiplicity of Mg, Si, S and Fe $K\alpha$ lines

ΔE (MeV/nucleon)	Mg		Si		S		Fe	
	H-like	He-like	H-like	He-like	H-like	He-like	H-like	He-like
0.5 - 1.0	0.21E-02	0.31E-01	-	0.38E-01	-	0.34E-02	-	-
1.0 - 1.5	0.11E+00	0.12E+01	0.58E-02	0.62E+00	0.30E-03	0.11E+00	-	-
1.5 - 2.0	0.66E+00	0.37E+01	0.73E-01	0.17E+01	0.69E-02	0.52E+00	-	0.22E-03
2.0 - 2.5	0.14E+01	0.39E+01	0.30E+00	0.23E+01	0.44E-01	0.11E+01	-	0.17E-02
2.5 - 3.0	0.17E+01	0.24E+01	0.64E+00	0.20E+01	0.14E+00	0.14E+01	-	0.72E-02
3.0 - 3.5	0.15E+01	0.11E+01	0.90E+00	0.14E+01	0.29E+00	0.14E+01	-	0.20E-01
3.5 - 4.0	0.12E+01	0.50E+00	0.97E+00	0.85E+00	0.45E+00	0.12E+01	0.22E-03	0.42E-01
4.0 - 4.5	0.86E+00	0.23E+00	0.89E+00	0.48E+00	0.56E+00	0.86E+00	0.68E-03	0.72E-01
4.5 - 5.0	0.64E+00	0.11E+00	0.76E+00	0.26E+00	0.60E+00	0.59E+00	0.17E-02	0.11E+00
5.0 - 6.0	0.85E+00	0.84E-01	0.11E+01	0.23E+00	0.11E+01	0.62E+00	0.11E-01	0.32E+00
6.0 - 7.0	0.51E+00	0.26E-01	0.72E+00	0.80E-01	0.85E+00	0.25E+00	0.30E-01	0.44E+00
7.0 - 8.0	0.32E+00	0.97E-02	0.47E+00	0.31E-01	0.61E+00	0.10E+00	0.65E-01	0.51E+00
8.0 - 9.0	0.22E+00	0.41E-02	0.32E+00	0.13E-01	0.44E+00	0.46E-01	0.11E+00	0.51E+00
9.0 - 10.0	0.15E+00	0.19E-02	0.23E+00	0.64E-02	0.31E+00	0.22E-01	0.16E+00	0.45E+00
10.0 - 12.0	0.19E+00	0.15E-02	0.29E+00	0.50E-02	0.40E+00	0.17E-01	0.42E+00	0.65E+00
12.0 - 14.0	0.11E+00	0.46E-03	0.17E+00	0.16E-02	0.23E+00	0.54E-02	0.45E+00	0.34E+00
14.0 - 16.0	0.66E-01	0.17E-03	0.10E+00	0.61E-03	0.15E+00	0.20E-02	0.39E+00	0.16E+00
16.0 - 18.0	0.43E-01	-	0.67E-01	0.26E-03	0.97E-01	0.88E-03	0.30E+00	0.76E-01
18.0 - 20.0	0.29E-01	-	0.46E-01	0.12E-03	0.67E-01	0.41E-03	0.23E+00	0.37E-01
20.0 - 25.0	0.42E-01	-	0.67E-01	0.10E-03	0.98E-01	0.36E-03	0.36E+00	0.32E-01
25.0 - 30.0	0.21E-01	-	0.33E-01	-	0.50E-01	-	0.19E+00	0.79E-02
30.0 - 35.0	0.12E-01	-	0.18E-01	-	0.28E-01	-	0.11E+00	0.25E-02
35.0 - 40.0	0.73E-02	-	0.11E-01	-	0.17E-01	-	0.71E-01	0.96E-03
40.0 - 45.0	0.48E-02	-	0.69E-02	-	0.11E-01	-	0.48E-01	0.42E-03
45.0 - 50.0	0.33E-02	-	0.46E-02	-	0.74E-02	-	0.33E-01	0.20E-03
50.0 - 55.0	0.23E-02	-	0.32E-02	-	0.52E-02	-	0.24E-01	0.11E-03
55.0 - 60.0	0.17E-02	-	0.23E-02	-	0.38E-02	-	0.18E-01	-
60.0 - 65.0	0.13E-02	-	0.17E-02	-	0.28E-02	-	0.14E-01	-
65.0 - 70.0	0.98E-03	-	0.13E-02	-	0.21E-02	-	0.11E-01	-
TOTALS	10.62	13.31	8.20	10.13	6.59	8.10	3.05	3.79

Table 5. Energies in keV of K X-ray lines from fast ions.
From Kelly (1987)

Projectiles	H-like		He-like	
	$K\alpha$ line	$K\beta$ line	$K\alpha$ line	$K\beta$ line
C	0.37	0.44	0.31	0.35
N	0.50	0.59	0.43	0.50
O	0.65	0.77	0.57	0.67
Ne	1.02	1.21	0.92	1.07
Mg	1.47	1.74	1.35	1.58
Si	2.01	2.38	1.86	2.18
S	2.62	3.11	2.46	2.88
Fe	6.97	8.25	6.70	7.88

Table 6. Energies in keV of K X-ray lines from ambient ions.

Elements	$E_{K\alpha}$	$E_{K\beta}$
C	0.29	-
N	0.40	-
O	0.53	-
Ne	0.85	-
Mg	1.25	-
Si	1.74	1.84
S	2.31	2.47
Ar	2.95	3.19
S	3.69	4.01
Fe	6.40	7.06

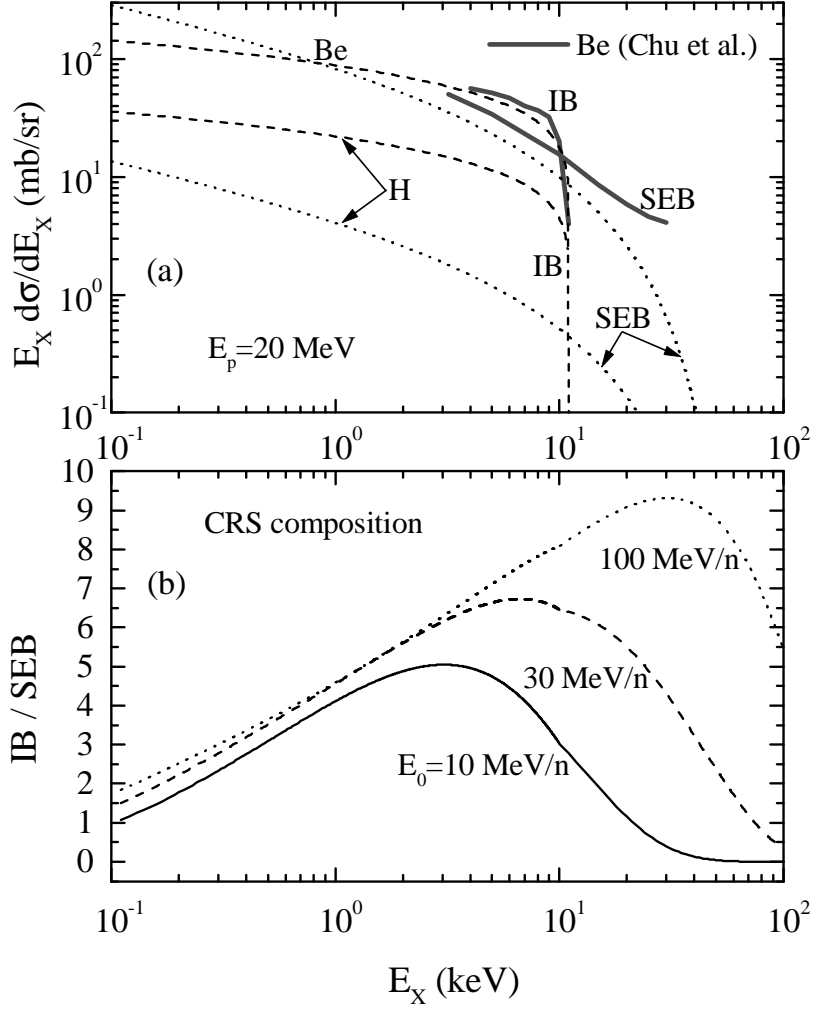


Fig. 1.— (a): Continuum X-ray production cross sections by a 20 MeV proton beam. The Chu et al. (1981) data (solid curves) are for X-rays observed from a Be target at 90° to the beam; the calculations, for both Be and H targets, are angle averaged; IB - inverse bremsstrahlung; SEB - secondary electron bremsstrahlung. (b): Ratio of the inverse bremsstrahlung (IB) to the secondary electron bremsstrahlung (SEB) productions, calculated from equation (1), for accelerated particle with CRS composition and spectra given by equation (2) and interacting with an ambient medium of solar composition.

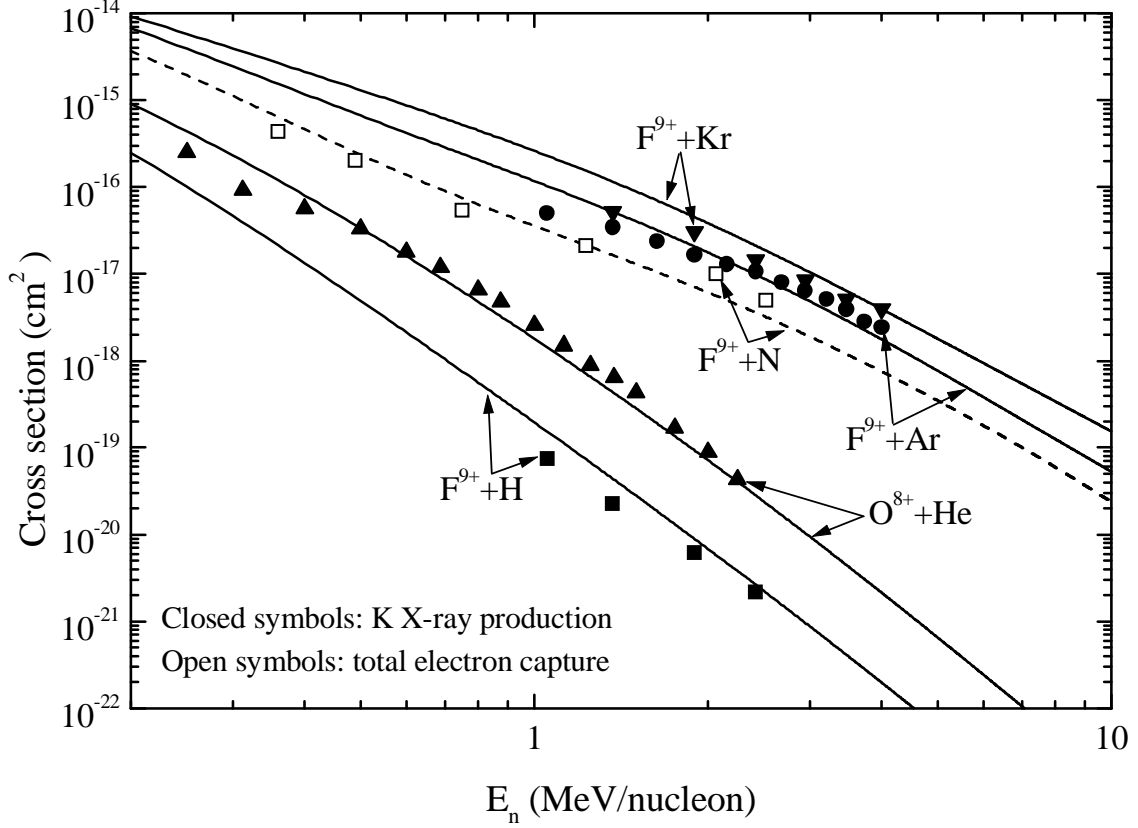


Fig. 2.— Charge exchange cross sections. The sources of the K X-ray production data are: $F^{9+} + H$ – Hopkins, Little & Clue (1976a); $O^{8+} + He$ – Guffey, Ellsworth & Macdonald (1977); $F^{9+} + Ar$ and $F^{9+} + Kr$ – Hopkins et al. (1976b). The $F^{9+} + N$ total electron capture data is from Macdonald et al. (1972). The theoretical curves employ the Nikolaev (1967) formalism with a single normalization constant of 0.1 for the five different cross sections; solid curves – K X-ray production cross sections; dashed curve – total electron capture cross section.

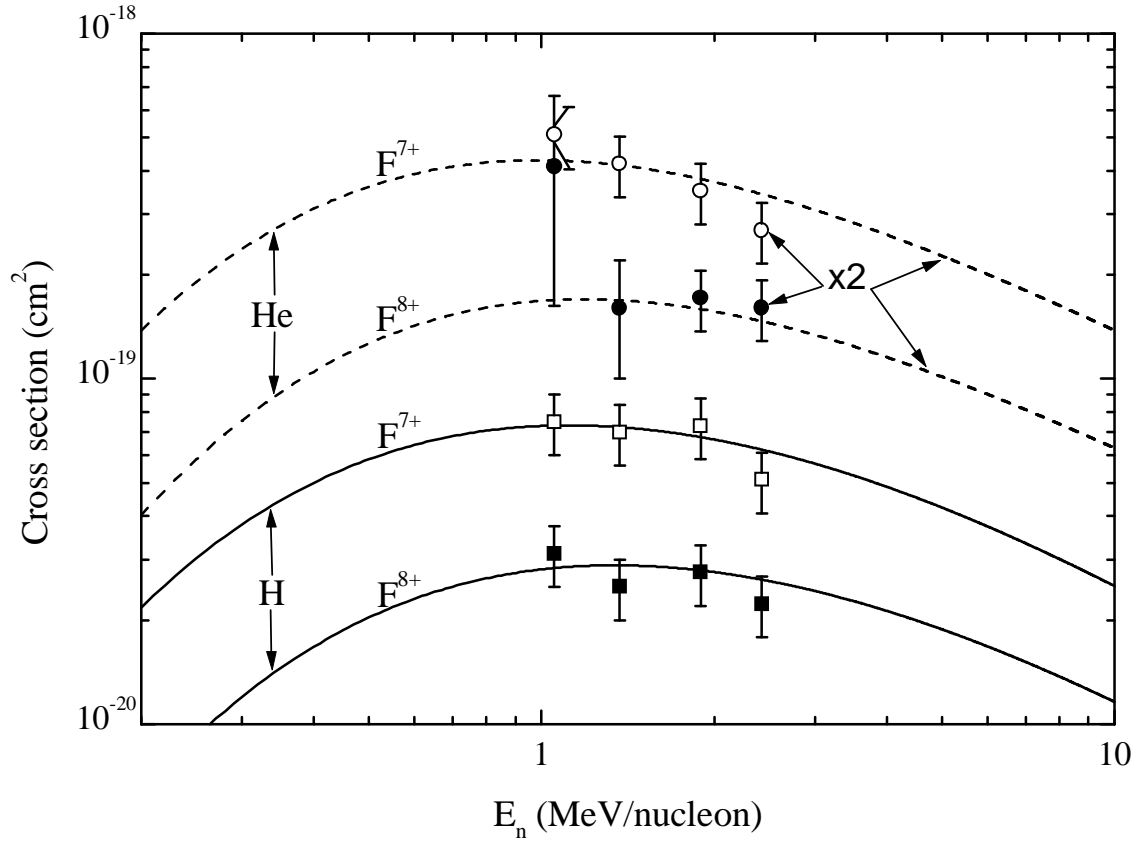


Fig. 3.— Excitation cross sections for fast F^{8+} and F^{7+} interacting in H and He. The data are from Hopkins et al. (1976a). The curves were obtained by using the plane-wave-Born-approximation (Bates 1962).

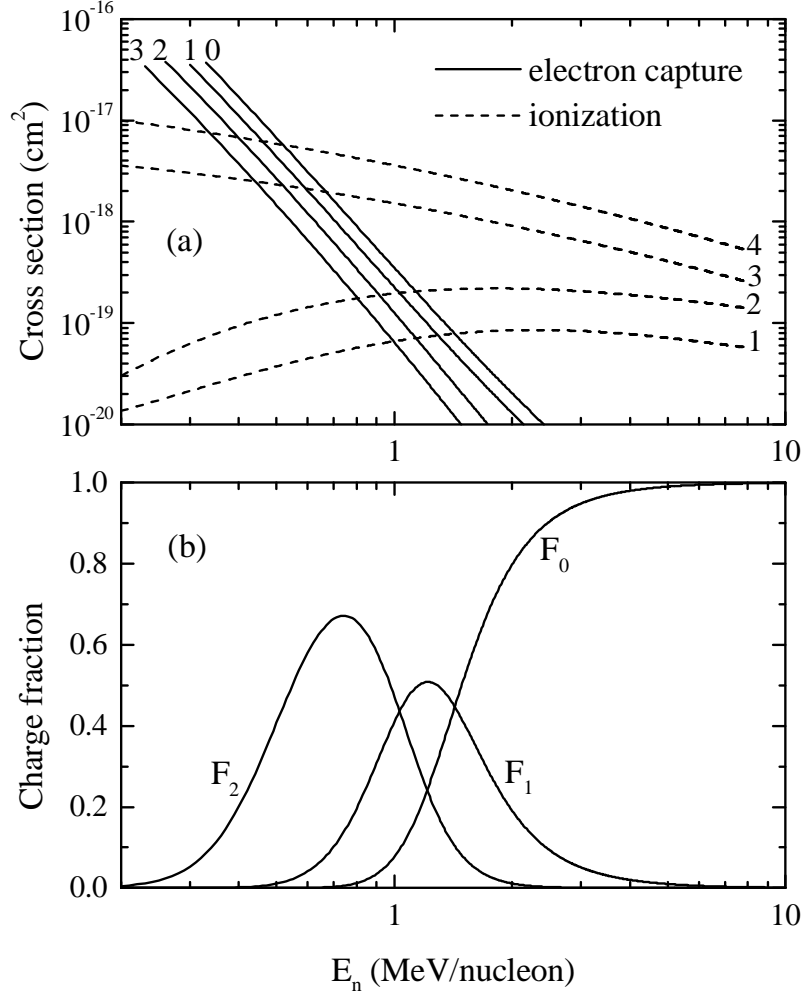


Fig. 4.— (a): Electron capture and ionization cross sections as a function of kinetic energy per nucleon, of fast O interacting in an ambient medium of solar composition. Each curve is labeled with the number of bound electrons of the incident O (i.e. before the collision). (b): Equilibrium charge fractions as a function of kinetic energy of fast O in a neutral medium of solar composition.

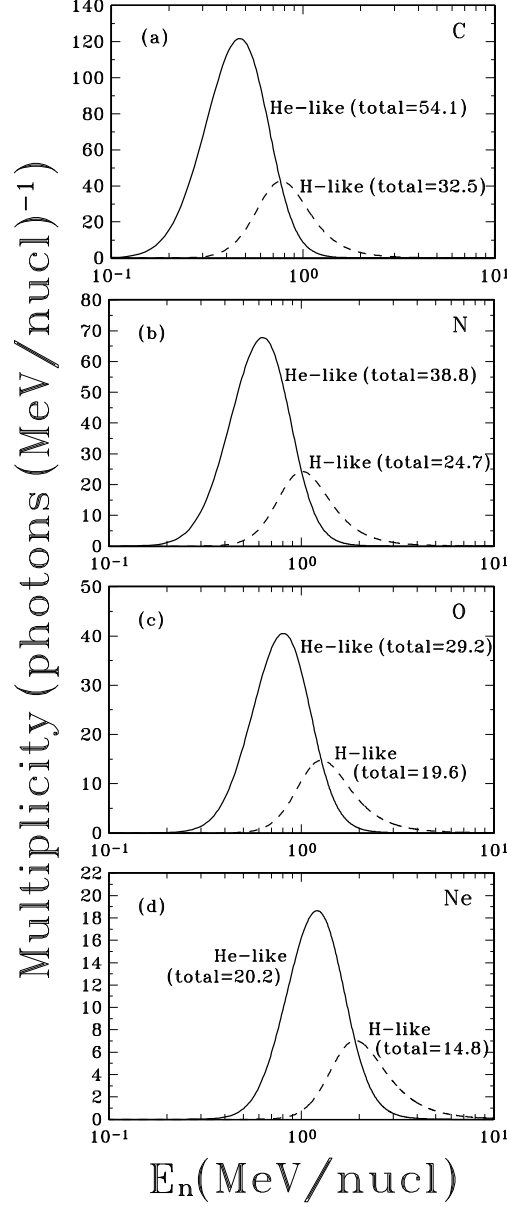


Fig. 5.— Differential $K\alpha$ X-ray line multiplicities for H-like and He-like fast C, N, O and Ne slowing down in an ambient medium with solar abundances as functions of the projectile kinetic energy per nucleon E_n . The same multiplicities are listed in Table 3 and the line centroids are given in Table 5. The $K\beta$ multiplicities are 25% of the corresponding $K\alpha$ multiplicities.

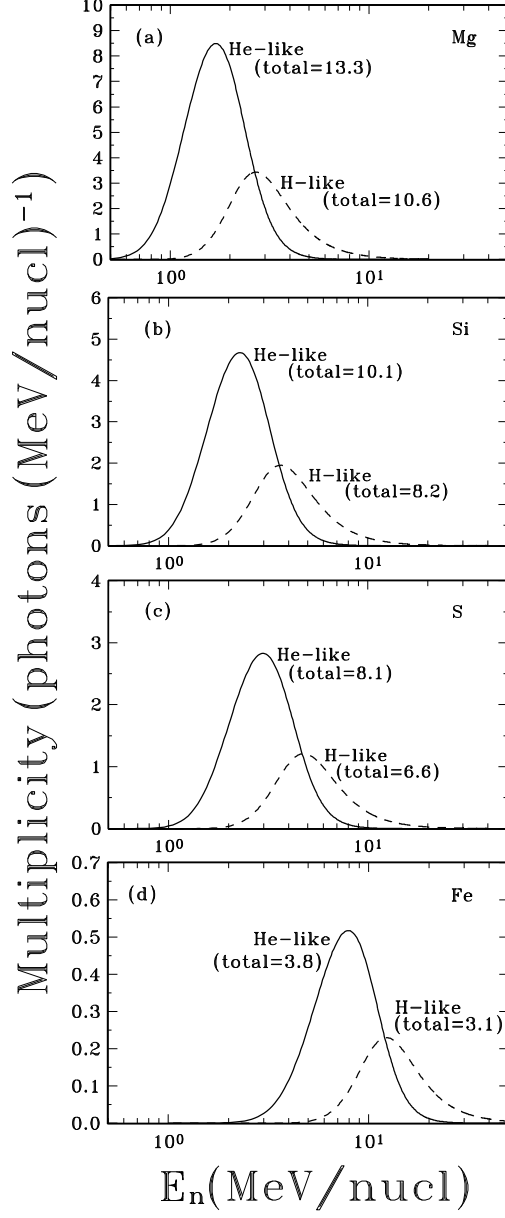


Fig. 6.— Differential K α X-ray line multiplicities for H-like and He-like fast Mg, Si, S and Fe slowing down in an ambient medium with solar abundances as functions of the projectile kinetic energy per nucleon E_n . The same multiplicities are listed in Table 4 and the line centroids are given in Table 5. The K β multiplicities are 25% of the corresponding K α multiplicities.

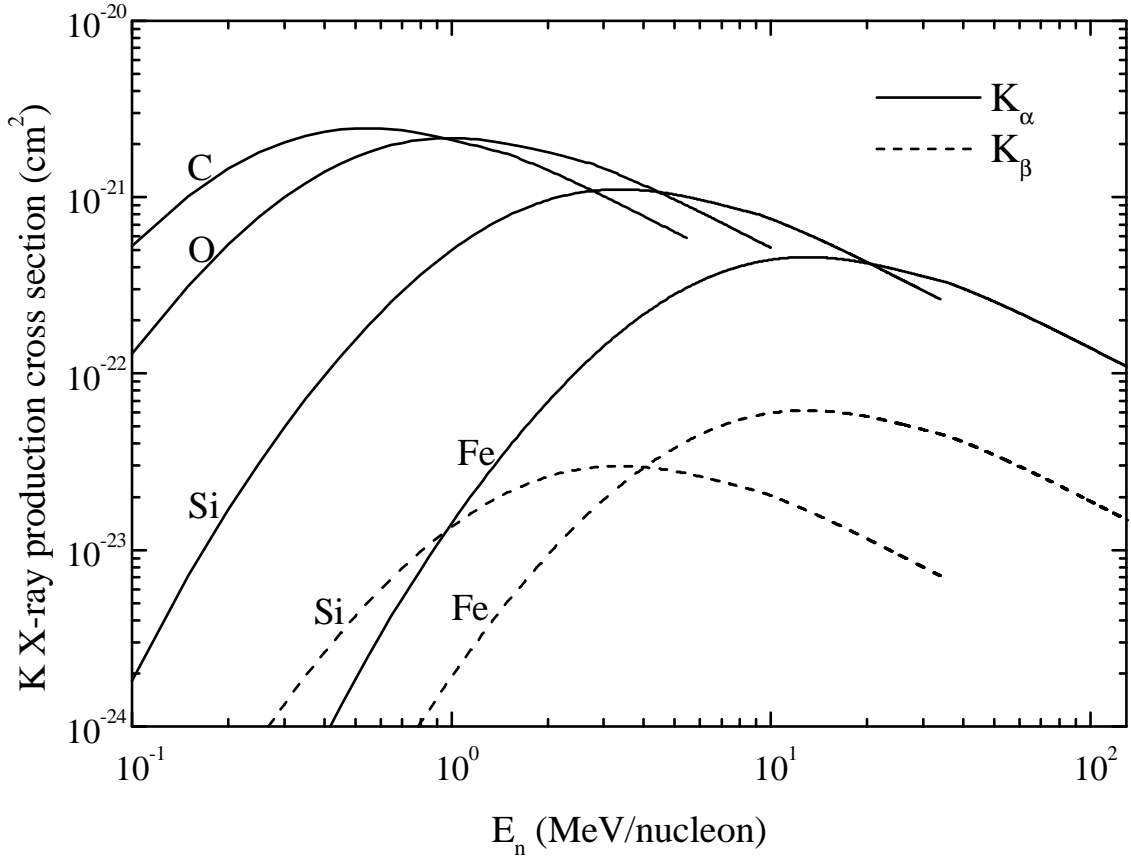


Fig. 7.— Cross sections for the production of K X-ray lines for fast protons interacting with ambient neutral C, O, Si and Fe. We do not consider $K\beta$ X-rays from Mg and lighter atoms because such atoms in their ground state do not have $3p$ electrons.

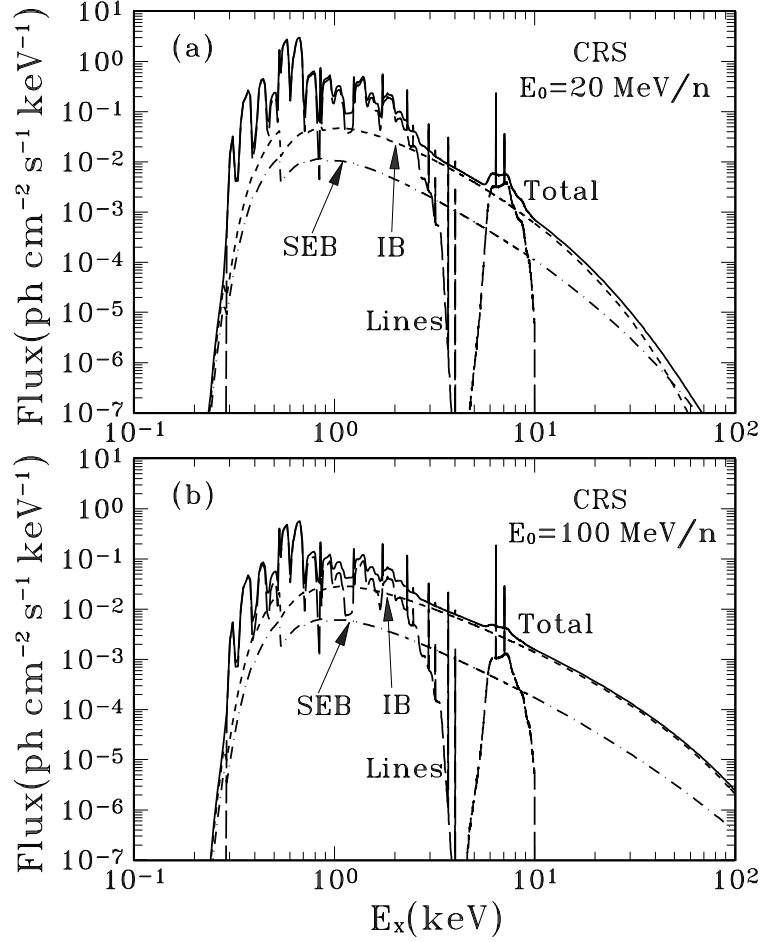


Fig. 8.— X-ray flux for the CRS composition with two values of E_0 . The calculations are normalized to a 3-7 MeV nuclear gamma-ray flux of $10^{-4} \text{ photons cm}^{-2} \text{s}^{-1}$. Photoelectric absorption is taken into account with a H column density of $3 \times 10^{21} \text{ cm}^{-2}$. IB - inverse bremsstrahlung; SEB - secondary electron bremsstrahlung.

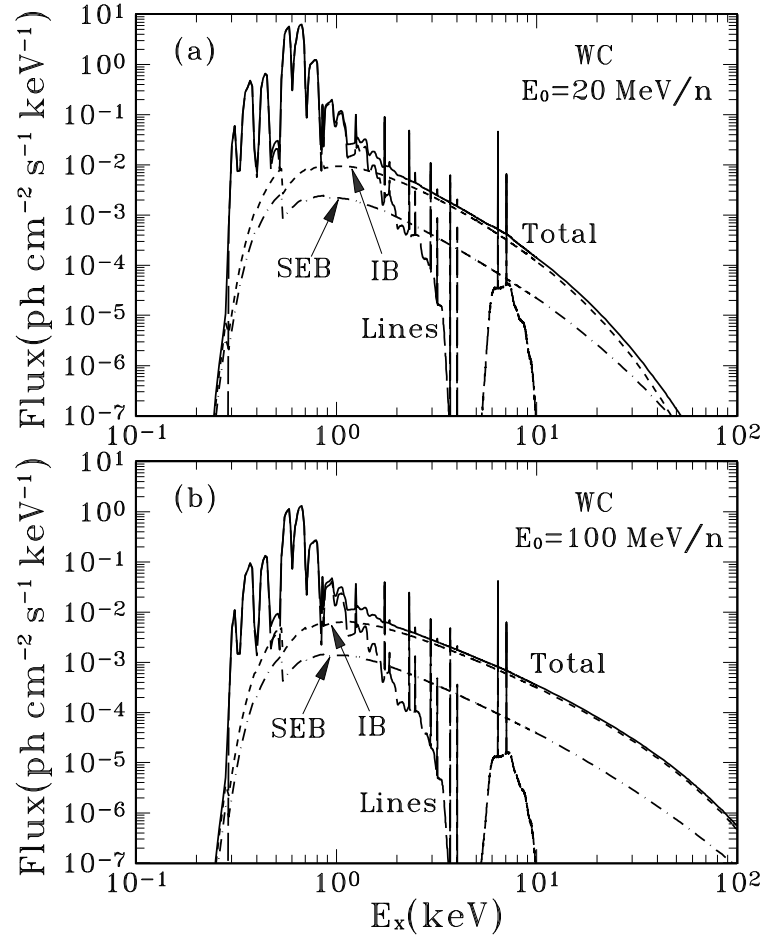


Fig. 9.— Same as Figure 8 but for the WC composition.

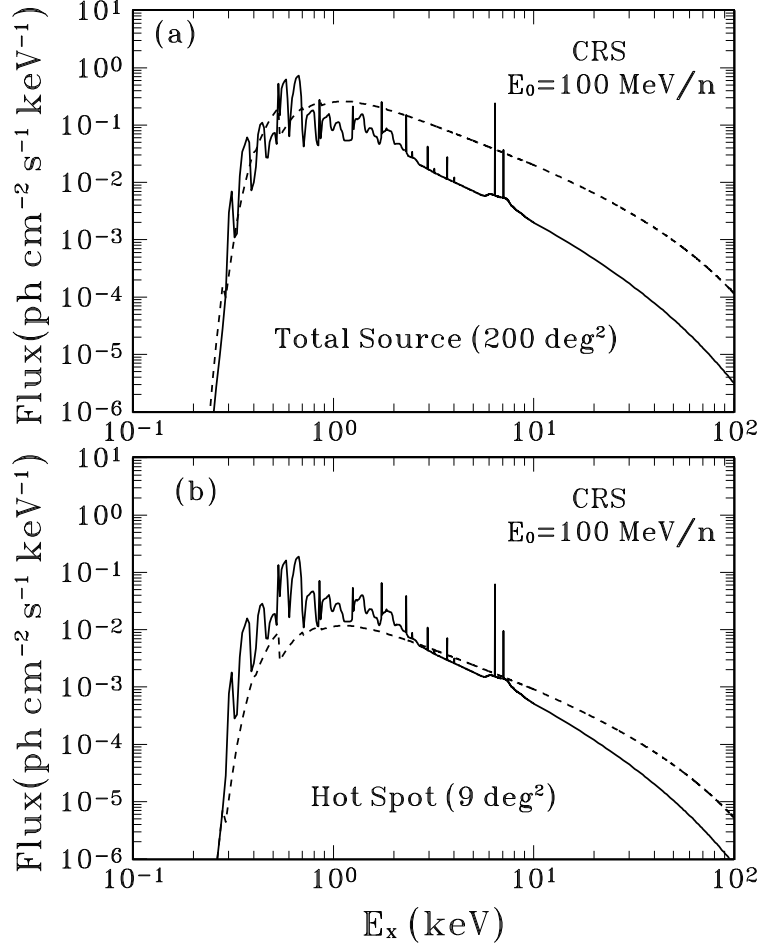


Fig. 10.— Solid curves – calculated X-ray fluxes from Orion from fast particle interactions for the CRS composition; dashed curves – extragalactic X-ray background flux. Panel (a) – calculated X-ray flux normalized to the total observed 3-7 MeV nuclear gamma-ray flux from Orion, 1.28×10^{-4} photons cm⁻² s⁻¹, assumed to be distributed over 200 deg²; panel (b) – calculated X-ray flux normalized to the observed nuclear gamma-ray flux of 3.3×10^{-5} photons cm⁻² s⁻¹ from a hot spot in Orion of assumed size 9 deg² centered at $l^{\text{II}}=213.6^\circ$, $b^{\text{II}}=-15.7^\circ$. The extragalactic flux is directly proportional to the assumed source size. Photoelectric absorption is taken into account with the same column density ($N_H=3 \times 10^{21}$ cm⁻²) for the X-rays produced in Orion and the extragalactic background. The same column density is used for the sources of the two panels.

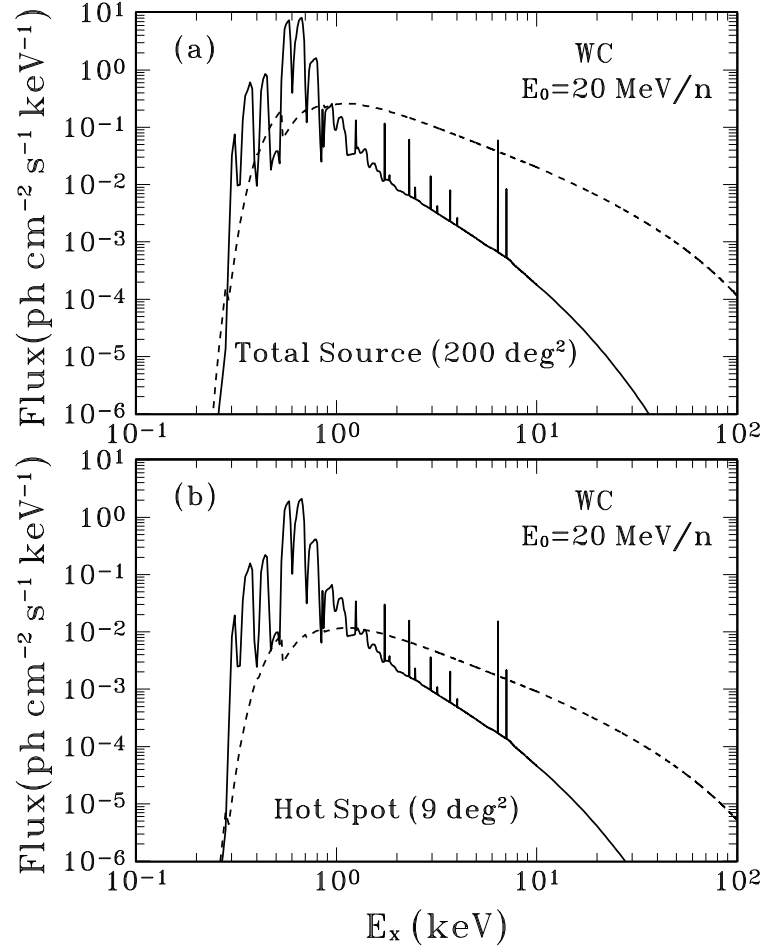


Fig. 11.— Same as Figure 10 but for the WC composition except that different values of E_0 are used in Figures 10 and 11.

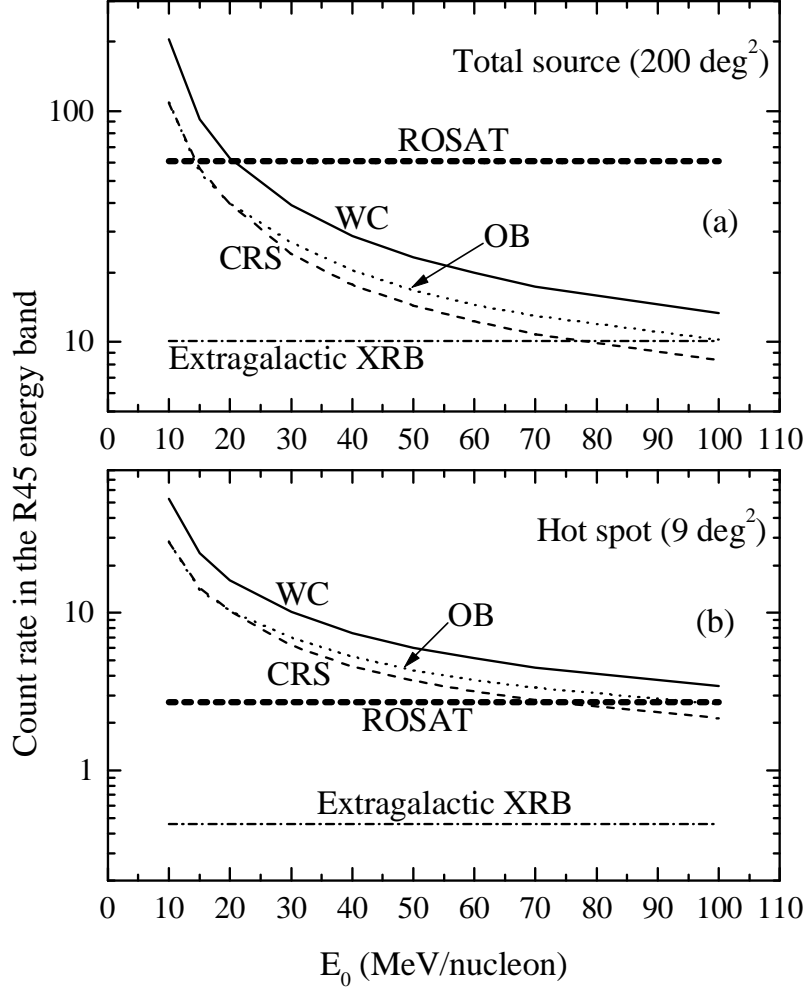


Fig. 12.— Comparison of the ROSAT R45 data for Orion with the calculated X-ray emission that is expected to accompany the observed nuclear gamma-ray emission, as a function of the characteristic energy E_0 [Eq. (2)] for the CRS, OB and WC compositions. The R45 energy band extends from 0.47 to 1.2 keV. The calculated X-ray spectra and the extragalactic X-ray background spectrum are convoluted with the ROSAT/PSPC response function to yield the R45 count rates. Panels (a) and (b) correspond to the same source parameters and column density as panels (a) and (b) in Figures 10 and 11.

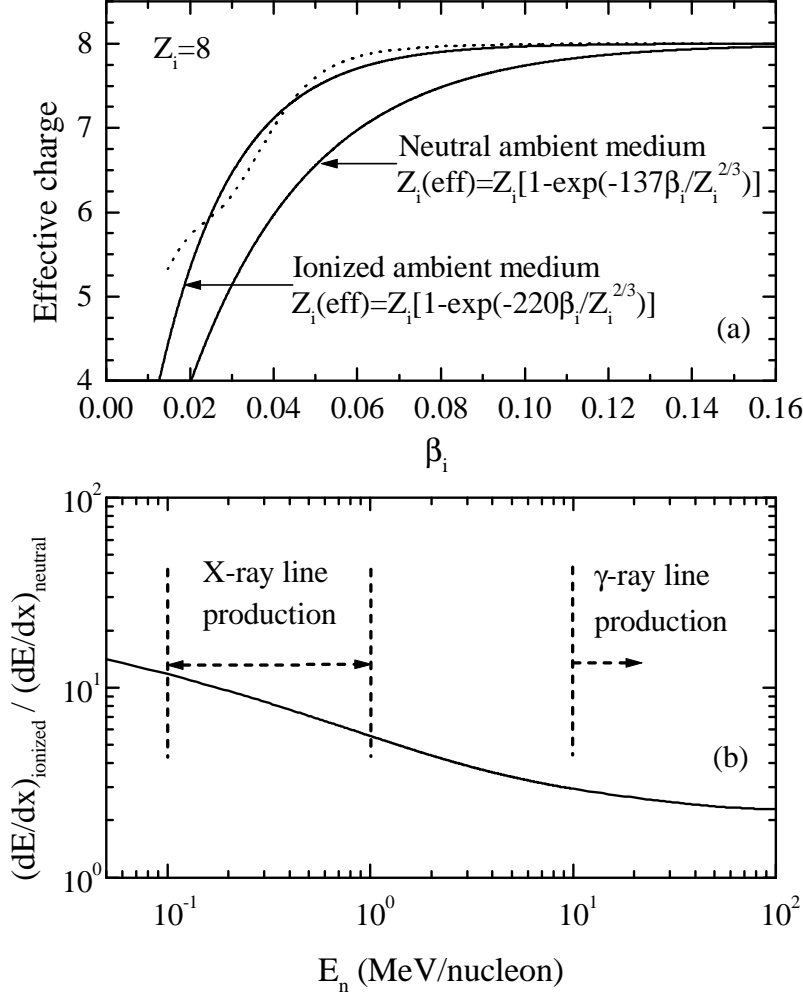


Fig. 13.— Effective charge and energy loss of fast O in an ionized ambient medium of solar composition compared with those in a neutral medium. Panel (a): dashed curve – calculated effective charge as a function of projectile velocity assuming that the ambient H and He are fully ionized and the heavier ambient elements are neutral; solid curves – adopted fits. The effective charge formula for fast ions in a neutral medium is from Pierce and Blann (1968). Panel (b): ratio of O energy loss in an ionized medium to the O energy loss in a neutral medium, as a function of kinetic energy/nucleon. The effective charges are calculated as in panel (a). The temperature of the ionized medium is 10^4 K. Also shown are the effective energy ranges of X-ray line and 3-7 MeV gamma-ray line productions from fast O in the ionized medium.

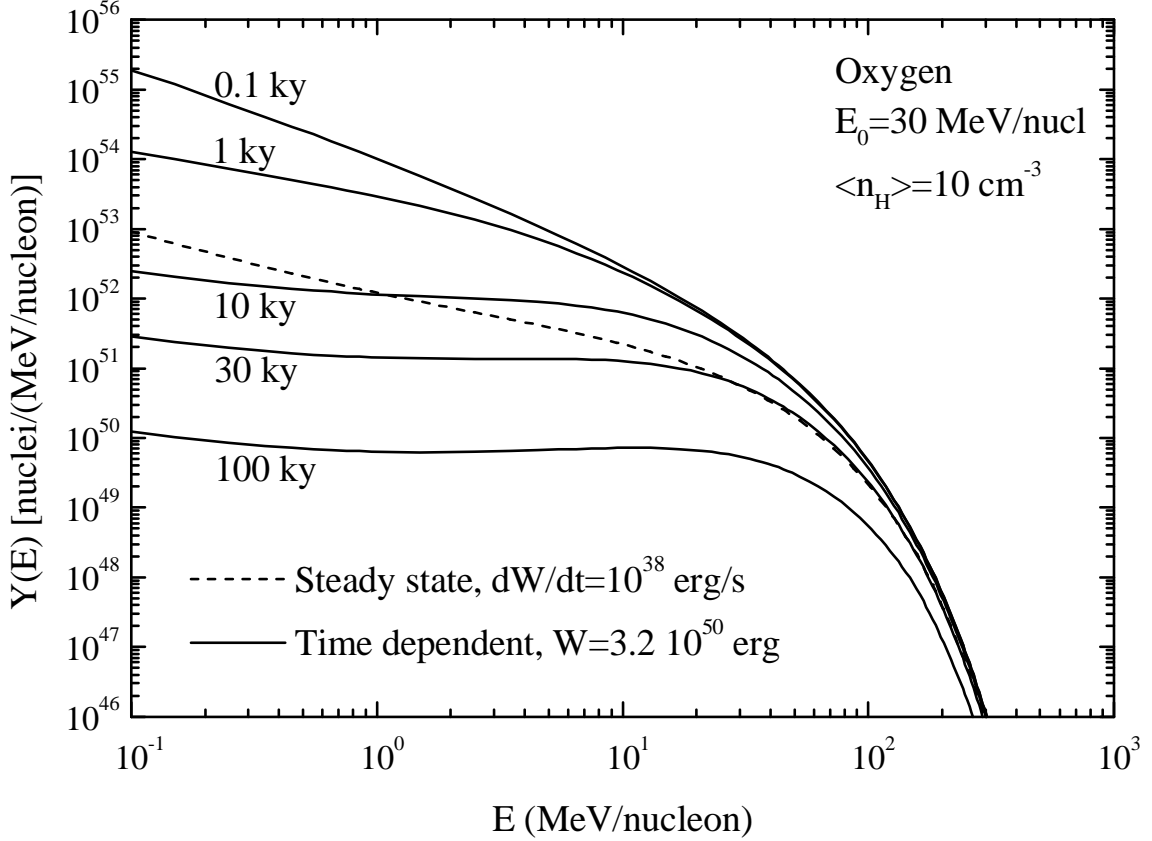


Fig. 14.— Comparison of the instantaneous, differential accelerated O numbers in the steady state and the time-dependent models. Dashed curve – differential equilibrium accelerated O number in the steady state model, normalized to a deposited power $dW/dt = 16 \int_0^\infty E \frac{dN}{dt}(E) dE$ of 10^{38} erg/s . This is the approximate power required to account for the observed nuclear gamma-ray lines, independent of the average ambient density $\langle n_H \rangle$. Solid curves – Time-dependent differential accelerated O number at different times ranging from $0.1 \cdot 10^3$ to $100 \cdot 10^3$ years after the initial instantaneous injection, normalized to a total deposited energy $W = 16 \int_0^\infty E Q(E) dE$ of $3.2 \cdot 10^{50} \text{ erg}$. In 10^5 years the deposited energy for the steady state model will equal the total deposited energy for the time-dependent model.